Towards Intra-Operative Dosimetry for Prostate Brachytherapy: Improved Seed Detection and Registration to Ultrasound Using Needle Detection

by

Julio Lobo

Engineering Physics, University of British Columbia, 2010

A THESIS SUBMITTED IN PARTIAL FULFILLMENT
OF THE REQUIREMENTS FOR THE DEGREE OF

Master of Applied Science

in

THE FACULTY OF GRADUATE STUDIES

(Electrical and Computer Engineering)

The University Of British Columbia

(Vancouver)

October 2012

Abstract

Errors in seed placement during low dose rate prostate brachytherapy can result in over-treating healthy tissue and/or under-treating cancer cells. In a standard treatment procedure, seeds are implanted according to a planned seed distribution. This pre-operative plan (pre-plan) is created using an ultrasound volume scan taken about two weeks earlier. Errors in seed placement can occur due to changes in prostate structure during those two weeks, and from seed displacement during and after the actual operation.

This thesis presents methods of seed localization that are suitable for both post-operative and intra-operative use. The techniques can be applied to the imaging modalities used in the current operation setup to implement a method of intra-operative planning. This involves using Transrectal Ultrasound (TRUS) and C-arm X-ray Fluoroscopy (fluoro) data to monitor the seed positions relative to the current target volume during an operation.

Towards this goal, an automatic method of assigning seeds to their corresponding insertion needle tracks has been developed to match seeds between modalities so that seed displacements can be computed. This method can be applied to measure intra-operative misplacement, by comparing the desired positions to the actual positions computed from fluoro data, or post-implant movement, comparing the fluoro seed positions to those from post-implant Computed Tomography (CT) data. For the intra-operative and post-implant data, 99.31% and 99.41% of the seeds were correctly assigned, respectively. An average intra-operative seed displacement of 4.94±2.42 mm and a further 2.97±1.81 mm of post-implant movement is measured. This information reveals several directional trends and can be used to preemptively correct the pre-operative plan (pre-plan).

An extension of the seed matching algorithm is used to register fluoro to intra-operative ultrasound so that the seed positions and displacements can be viewed with respect to soft tissue features. An ultrasound volume can be acquired immediately prior to or during an operation, instead of weeks before, removing the errors in the pre-plan.

Looking to the future, an absolute elastography system is tested which can provide automatic delineation of the target volume and segmentation of the soft tissue features which is required to complete the intra-operative planning procedure.

Preface

Material from Chapter 2 was published in the International Journal of Medical Physics in Research and Practice: "Prostate implant reconstruction from C-arm images with motion-compensated tomosynthesis". The work was co-authored by Ehsan Dehghan (first author), Mehdi Moradi, Xu Wen, Daniel French, Julio Lobo, W. James Morris, Septimiu E. Salcudean, and Gabor Fichtinger [1]. The original back-projection code was written by Daniel French before being optimized to run in real time and incorporated into a Graphical User Interface by the author. The seed reconstruction results from the patient study presented in this work were provided by Ehsan Dehghan and used for further investigation in Chapters 3 and 4 of this thesis.

A summary of the methods and results from Chapter 3 and 4 was accepted for publication in the conference for Medical Image Computing and Computer Assisted Intervention (MICCAI) under the title "Quantifying stranded implant displacement following prostate brachytherapy". The work was co-authored by Mehdi Moradi, Nick Chng, Ehsan Dehghan, William J. Morris, Gabor Fichtinger, Septimiu Salcudean [2]. A detailed algorithm description and further analysis was later published by IEEE in the journal IEEE Transactions on Medical Imaging under the title "Use of Needle Track Detection to Quantify the Displacement of Stranded Seeds Following Prostate Brachytherapy" with the same authors [3]. The author

---

[1]E. Dehghan, M. Moradi, X. Wen, D. French, J. Lobo, W. J. Morris, S. Salcudean and G. Fichtinger. Prostate implant reconstruction from C-arm images with motion-compensated tomosynthesis. *Medical Physics*, pages 5290-5303, 2011

[2]J. Lobo, M. Moradi, N. Chng, E. Dehghan, W. J. Morris, G. Fichtinger and S. Salcudean. Quantifying stranded implant displacement following prostate brachytherapy. *Medical Image Computing and Computer Assisted Intervention*, pages 307-314, 2011

[3]J. Lobo, M. Moradi, N. Chng, E. Dehghan, W. J. Morris, G. Fichtinger and S. Salcudean.

assisted in patient data collection and performed the data analysis and algorithm development described in these chapters.

The fluoro to ultrasound registration described in Chapter 4 was accepted for publication in the conference for Medical Image Computing and Computer Assisted Intervention (MICCAI) under the title "Towards intra-operative prostate brachytherapy dosimetry based on partial seed localization in ultrasound and registration to C-arm fluoroscopy". The work was co-authored by Mehdi Moradi (first author) Sara Mahdavi, Sanchit Deshmukh, Julio Lobo, Ehsan Dehghan, Gabor Fichtinger, W. James Morris and Septimiu Salcudean [4]. The algorithms were extended and applied to a larger dataset and then published by IEEE in IEEE Transactions on Biomedical Engineering under the title "Seed localization in Ultrasound and Registration to C-Arm Fluoroscopy Using Matched Needle Tracks for Prostate Brachytherapy" with the same authors [5]. The author provided fluoro needle intersections and developed initial 2D registration techniques for this process.

Fluoro images, CT scans, and ultrasound data was collected from patients undergoing prostate brachytherapy as part of a study for Visualization and Real-Time Dosimetry for Prostate. This study was approved by the University of British Columbia (UBC) Research Ethics Board. The UBC CREB number of this study is H06-70146. Tim Salcudean is the principle investigator for this study and co-investigators include Reza Zahiri, Xu Wen, W. James Morris, and Daniel French. Nick Chng assisted with coordination of the patient study, with data collection and provided pre-plan and CT reconstructions.

The code used to compute and save data required for elastography computation in Chapter 5 was written by Ali Baghani, Hani Eskandari, Weiqi Wang, Daniel Da Costa and Neerav Patel. The algorithms used were co-developed by Ali Bahgani,

Use of Needle Track Detection to Quantify the Displacement of Stranded Seeds Following Prostate Brachytherapy. *IEEE Transactions on Medical Imaging*, volume 31, issue 3, pages 738-748, 2012

[4]M. Moradi, S. Mahdavi, S. Deshmukh, J. Lobo, E. Dehghan, G. Fichtinger, W. J. Morris, S. E. Salcudean. Towards intra-operative prostate brachytherapy dosimetry based on partial seed localization in ultrasound and registration to C-arm fluoroscopy. *Medical Image Computing and Computer Assisted Intervention*, pages 291-298, 2011

[5]M. Moradi, S. Mahdavi, S. Deshmukh, J. Lobo, E. Dehghan, G. Fichtinger, W. J. Morris, S. E. Salcudean. Seed localization in Ultrasound and Registration to C-Arm Fluoroscopy Using Matched Needle Tracks for Prostate Brachytherapy. *IEEE Transactions on Biomedical Engineering*, volume 59, issue 9, pages 2558-2567, 2012

Table of Contents

List of Tables

List of Figures

Glossary

fluoro C-arm X-ray Fluoroscopy

CT Computed Tomography

TRUS Transrectal Ultrasound

pre-plan pre-operative plan

RF Radio Frequency

RP Reflected Power

QA Quality Assurance

ABS American Brachytherapy Society

MRI Magnetic Resonance Imaging

OR Operating Room

LFE Local Frequency Estimators

TWE Travelling Wave Expansion

UI User Interface

GUI Graphical User Interface

ROI Region of Interest

ICP Iterative Closest Point

GMM Gaussian Mixture Model

RANSAC RANdom Sample Consensus

DRR Digitally Reconstructed Radiography

ASM Active Shape Modeling

GPU Graphical Processing Unit

IQ Inphase Quadrature

bNED biochemical No Evidence of Disease

PSA Prostate-Specific Antigen

Acknowledgments

I would like to thank my supervisor, Tim Salcudean, for his continual advice and support. The wide range of exposure (not to mention the cool toys!) that you can only get at the Robotics and Control Lab at UBC is a testament to your commitment to research and willingness to always provide support for new ideas.

I would also like to thank Mehdi Moradi for all his help with so much of this work. Thank you for reading through my paper so many times and helping with the whole publication process.

Nick Chng was extremely helpful with coordinating the prostate brachytherapy project. A majority of the patient data acquired for this study could not have been done without your help and provision. You are always willing to provide support and insight which I used abundantly! I would like to thank Xu Wen as well, who also helped coordinate the brachytherapy patient study and collect data.

The accurate fluoro reconstruction were generously provided by Ehsan Dehghan who also helped me with the publication process.

I would like to thank Dr. James Morris for his support of the brachytherapy project and also for the valuable information used to help with the seed displacement trend analysis.

I would also like to thank Ali Baghani and Hani Eskandari for all their help with the elastography component of this thesis. Both of you were very considerate and willing to dedicate time to help me understand the software. Thanks goes to Weiqi Wang as well, who had a huge part in developing the code, both during the conversion to CUDA before I started on the project and then during the restructuring to work with the BK machine. He also helped in transporting the system back and forth from the hospital. Thank you also to Samuel Frew, who designed and

built the shaker control box which is a vital part of the elastography system.

The data collection process for the elastography patient study was made possible by Omid Mohareri. Thank you for organizing this and also for waking up so early in the morning got collect the data with me! The process was also supported by Dr. Larry Golderburg and the nurses at Vancouver General Hospital (VGH) who helped us out a lot.

A big thanks also goes to thank Jenna Thompson, Paolo Lobo and Philip Edgcumbe for taking time to read through sections of this thesis while I was writing it.

Finally, I wish to thank my parents and all my family back home in Kenya for all the support they have provided and continue to provide! It's difficult being so far away but you have always made me feel like I can and should achieve the best.

Dedication

I would like to dedicate this thesis to my grandfather, Antonio Caetano Sylvestre Lobo, who passed away earlier this year with prostate cancer. Thank you for teaching me to be determined and to always strive for perfection!

Chapter 1

Introduction

Prostate cancer is the most common cancer in men in the Americas and Africa. It is also the leading cause of cancer deaths in Africa and in the low to middle income regions of the Americas [44].

There are a wide range of treatment techniques for prostate cancer ranging from active surveillance to radical prostatectomy. Low dose, permanent implant, prostate brachytherapy is a procedure that has been shown to effectively treat men with prostate cancer [49]. It involves the insertion of radioactive seeds, using needles, into the prostate through the perineum. In most current procedures, a Transrectal Ultrasound (TRUS) scan - taken several days to weeks before a brachytherapy procedure - is used to create a pre-operative plan (pre-plan) which defines how the seeds are to be distributed within the prostate and surrounding regions. The plan is made under the constraint of placing individual seeds at varying depths along several parallel lines so that it can be replicated intra-operatively using needle insertions.

The treatment relies on accurate placing of the radioactive seeds to sufficiently irradiate tumours while sparing non-cancerous tissue. Errors in seed position lead to poor implant quality and can arise from a number of different reasons. Firstly, there can be variations in the shape and position of prostate, as well as the cancerous regions within it, at the time of an operation as compared to the pre-plan conditions. The prostate structure can change due to muscle relaxation after the patient is under anaesthesia, anti-androgen hormone therapy that is sometimes used

to shrink the prostate volume, or aggressive tumour growth. Secondly, even with a perfect pre-plan, misplacement of seeds can occur due to prostate movement [40] and/or needle deflection during insertion. Lastly, movement of the seeds *after* an operation (post-implant movement) can occur due to prostate inflammation [83] or change in patient position.

Research has suggested that one of the ways of reducing the errors mentioned above is to use *intra-operative planning* [52, 59]. This is the process where a plan is made and modified in the Operating Room (OR) compensating for any unexpected misplacements or predictable movements during the operation. This necessarily requires that position and size of the tumours, as well as the location of the seeds with respect to the tumours, be known at any given time *during* an operation. Clearly this means that more *intra-operative* data (data acquired during the operation) needs to be collected and processed. When collecting intra-operative data, it must not take too much time or space so that the implantation procedure itself is affected as little as possible. It is worth while therefore, to examine at the current brachytherapy setup to identify potential improvements in seed placement accuracy.

During a regular brachytherapy procedure, TRUS imaging is used for guidance with the occasional use of C-arm X-ray Fluoroscopy (fluoro) images (Figures 2.2 and 3.1 show the brachytherapy setup with fluoro and TRUS) . The two imaging modalities are used together because they can both be incorporated into the operating procedure without limiting the space and accessibility to the patient but cannot individually provide all the information needed. The prostate and other soft tissue structures are easily visible in TRUS images but the brachytherapy seeds are not easy to identify. This is because they are highly acoustically reflective and shadow each other and are easily confused with reflections from calcifications. In contrast, the seeds are clearly visible in fluoro images, which also have a much larger field of view, but the soft tissue features are not visible. The two imaging modalities therefore compliment each other perfectly. Figure 1.1 shows example fluoro and ultrasound images of the prostate. It would be useful to make use of the currently used imaging modalities to enhance the intra-operative data in order to minimize the displacement errors. This would improve the quality of the implants without complicating the standard procedure.
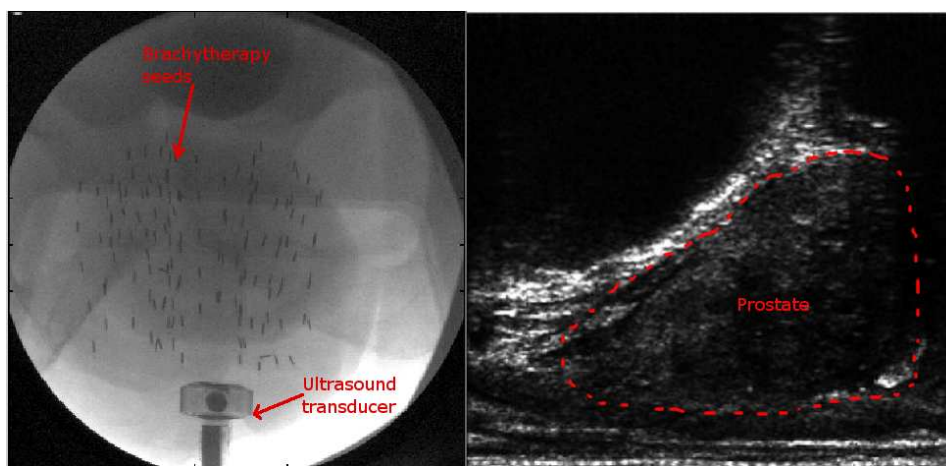
Figure 1.1: Example fluoro (left) and sagittal ultrasound (right) images that are taken during a routine brachytherapy procedure. The brachytherapy seeds can clearly be seen in the fluoro image, as well as the ultrasound transducer, but the prostate itself is not visible. In the TRUS image the prostate is visible (in the bottom right corner of the image) but there is a limited field of view.

It is possible to include other imaging modalities in the prostate brachytherapy procedure to provide intra-operative data such as the use of Magnetic Resonance Imaging (MRI) [70, 72] but these require a drastically different OR setup. Other solutions include the use of new flat panel C-arm fluoroscopy detectors to implement cone-beam Computed Tomography (CT) imaging which provides both high quality imaging of soft-tissue and accurate seed reconstruction [30, 66]. Both cone-beam CT and MRI are likely to become a standard part of future procedures but are more expensive in comparison to the current imaging modalities and not widely available. Therefore, it is valuable to assess the feasibility of using the currently used technology to help reduce the seed displacement errors. For the remainder of this document, the only intra-operative imaging modalities that will be analyzed will be TRUS and fluoro.

Returning to the issues that lead to errors in implant quality, the first concern is the possibility of the pre-plan being "out of date" due to changes in the shape and size of the prostate and the target regions within it. The solution to this is to

have a method of identifying these regions in the OR right before and during an operation. Since fluoro cannot image soft tissue this can only be done using TRUS. Several groups have studied a method of using TRUS volumes taken immediately before an operation to create a plan [47], called "Intra-operative pre-planning" by the American Brachytherapy Society (ABS) [52], and found it to dosimetrically favourable in comparison to the traditional pre-plan [12, 25, 64, 81]. However, this approach requires manual contouring of the prostate which takes up valuable time in the OR and only provides intra-operative information of the prostate and not the target regions within it.

It has been shown that the stiffness of abnormal tissue masses increases due to change in cell density [39] and so several research groups have investigated the use of elastography to detect cancer [38, 54, 56, 63]. This technique could allow automatic segmentation of the prostate as well as delineation of tumours in real-time. An extension to this is to use Local Frequency Estimators (LFE) or a Travelling Wave Expansion (TWE) to solve the inversion problem to obtain the absolute viscoelastic properties of the tissue described by Baghani *et al.* [9, 10]. Being able to locate target regions in real-time during brachytherapy also opens the door to treatment techniques such as focal therapy [2, 18, 50] which could further improve the treatment of prostate cancer by treating subregions of the prostate rather than the whole gland preserving healthy tissue.

Once the issue of an "out of date" pre-plan is solved the remaining issues that need addressing are seed misplacement during an operation and seed movement afterwards. In order to address these there needs to be a way of computing the undesirable seed displacements. Post-implant dosimetry for Quality Assurance (QA) is recommended by the American Brachytherapy Society [51] and is implemented at most medical clinics. Regular CT scans are used to look at post-implant seed distributions. If substantial implant errors are found, post-operative measures can be taken but this can lead to even more complications. It would be more beneficial reduce implant errors by using intra-operative planning [52, 55, 59] to detect and correct the errors during the operation. The most ideal form of intra-operative planning is "dynamic dose calculation" which requires continual localization of individual seeds [52, 59] to compare the real seed distribution with the desired one. Fluoro imaging can used to perform the intra-operative seed localization. The use of a

few fluoro images taken over a narrow angle to reconstruct the intra-operative seed positions has been performed by numerous groups successfully [31, 41, 67, 73–75]. In most cases. the reconstruction algorithms assume that the C-arm remains translationally fixed during the image acquisition. However, Dehghan *et al.* have developed a method of performing the reconstruction which compensates for the small amounts of motion that can be expected [16].

Once the intra-operative seed positions have been obtained, it is then necessary to identify the same seeds in pre-plan, intra-operative and post-implant conditions. Comparing pre-plan positions to intra-operative positions would give immediate feedback as to whether the seeds are implanted as expected. Intra-operative data and post-implant data can also be used to compute trends in both intra-operative misplacement and post-implant movement that can be used to guide future brachytherapy operations.

The final component needed for intra-operative planning is to register the intra-operative datasets to each other. More specifically, the computed 3D seed positions must be registered to the prostate volume. Registration between ultrasound and fluoro is a viable solution [21, 23, 68] to this. Moradi *et al.* present a complete method of computing partial seed volume reconstructions in ultrasound and using needle track detection to match the dataset to fluoro data without the need for fiducials or manual segmentation [48].

1.1 Thesis Objectives

This thesis describes techniques that use the current imaging modalities for prostate brachytherapy to: observe the target volume in real time, predict likely seed displacement just before insertion, and detect misplacements immediately after insertion. All of these processes are needed to provide true intra-operative planning for prostate brachytherapy. The main thesis objectives are as follows:

1. To develop a method to compute seed displacements by comparing seed clusters reconstructed from different modalities. Any displacement trends found from this study can be compensated during needle placement and the same algorithms can be used in real time to detect unexpected misplacements immediately.

2. To provide a method to register fluoro to ultrasound so that seeds and displacements can be viewed with respect to patient anatomy.

3. To develop an imaging system to display real-time viscoelastic properties of the prostate using ultrasound to allow delineation of the prostate and the cancerous regions within it.

For each of these objectives, the combination of *speed*, *accuracy* and degree of *automatism* needs to be analyzed to test the feasibility of intra-operative planning. These criteria are enforced by the high intensity setting that exists in the OR.

1.2 Thesis Outline

A major requirement for intra-operative planning is the ability to compute seed distributions during a procedure. Chapter 2 describes the setup used to obtain intra-operative patient data and the algorithm used to obtain the 3D positions of the brachytherapy seeds. For the system to be efficient in the OR it needs to be fully automatic. The steps taken to automatically process the images are described. Descriptions of the planned and post-implant datasets are also provided.

Chapter 3 describes a "Needle Track detection algorithm". It covers the methods used to group the seeds into their corresponding needles. This grouping allows seed matching to be performed by identifying corresponding needle groups in different datasets rather than identifying individual seeds. The key feature of this algorithm is that it can be applied over a wide range of datasets, including intra-operative fluoro data, to allow matching of seeds at different times and also between imaging modalities.

Chapter 4 presents two applications of the needle track detection algorithm. The first application is the computation of intra-operative and post-implant seed displacement. Intra-operative seed misplacement is measured by comparing intra-operative seed positions from fluoro data to those from the pre-plan. Similarly, post-implant seed movement is calculated by comparing the intra-operative seed positions to those from post-implant CT data. The displacement values are only truly useful if the reconstructed seed clouds are registered to the prostate itself, which is not visible in the fluoro or CT images. The second application of the

needle track detection algorithm is a method of performing this registration. Only a few strands are detectable in the ultrasound volume but registration is still possible [48].

Once the seed positions are found and registered to an ultrasound volume it is still necessary to segment the prostate, and the cancerous regions within it, in order to complete the planning process. An existing inversion algorithm [9] was used to reconstruct the viscoelastic properties of the prostate which allows for this segmentation. Chapter 5 describes how this algorithm was used for the first time with a BK Medical ultrasound machine (BK Medical, Herlev, Denmark) to obtain both phantom and patient data.

Finally, Chapter 6 describes the conclusions and contributions of this thesis as well as the future research directions.

Chapter 2

Intra-operative Seed Localization

2.1 Introduction

The success of intra-operative planning is heavily dependent upon the availability and reliability of the intra-operative data. Several different types of data are required to provide intra-operative planning for prostate brachytherapy. This data includes the ultrasound imaging used to view the prostate as well as the various methods of obtaining localized seed positions. Chapter 5 will address the process in which the prostate itself can be imaged while this chapter describes the techniques used to obtain pre-plan, intra-operative and post-implant reconstructions of the seed positions. The focus will be on the intra-operative seed positions since this area has the most potential for improvement since pre-operative and post-implant reconstructions are already accurate and do not need to be performed in real-time.

All the data for the seed reconstruction as well as the seed displacement analysis (Chapters 3 and 4) was taken from a patient study of 8 patients undergoing low dose, permanent implant, prostate brachytherapy at the British Columbia Cancer Agency (BCCA), Vancouver, Canada. Institutional Research Ethics Board approval and patient consent were acquired.

The Variseed planning software (Varian Medical, Palo Alto, CA) was used to export both the pre-plan seed positions as well as the post-implant CT seed positions. In some cases the radiation oncologists changed the plan adding "voodoo" (not part of the pre-plan) seeds and these were included in the pre-plan datasets

Table 2.1: Summary of the seed reconstruction data types and their uses.

Seed cloud reconstruction data type	Time of Acquisition	Use
Pre-plan	pre-operative	Used to compute misplacement during insertion by comparing with intra-operative fluoro data
Fluoro	intra-operative	Provides a complete reconstruction of the seed positions immediately after insertion
TRUS	intra-operative	Used to register intra-operative fluoro and ultrasound data
CT	post-implant	Used to compute post-implant seed movement trends by comparing with intra-operative fluoro data

used for this study.

Table 2.1 summarizes all the types of seed reconstructions datasets. The third column describes what each dataset is used for. It can be seen that all of these analyses require the use of the seed localization from intra-operative fluoroscopic data. These are the seed positions immediately after they are inserted, while the patient is still in the operating position. These positions can be computed in the middle of an operation and do not necessarily need to be computed after all the seeds are implanted.

The seed localization process in ultrasound will be presented first followed by a step-by-step description of the process required to reconstruct the seed positions in fluoro.

2.2 Method for Seed Localization in TRUS Volumes

Intra-operative seed positions computed from ultrasound data were obtained from a concurrent study by Moradi *et al.* [48]. Since it is extremely difficult to reconstruct all the seeds using ultrasound, even when manual segmentation is used [31], these seed positions are not used to compute displacements. They can be used, however, to register the ultrasound and fluoro datasets to each other so that displacements
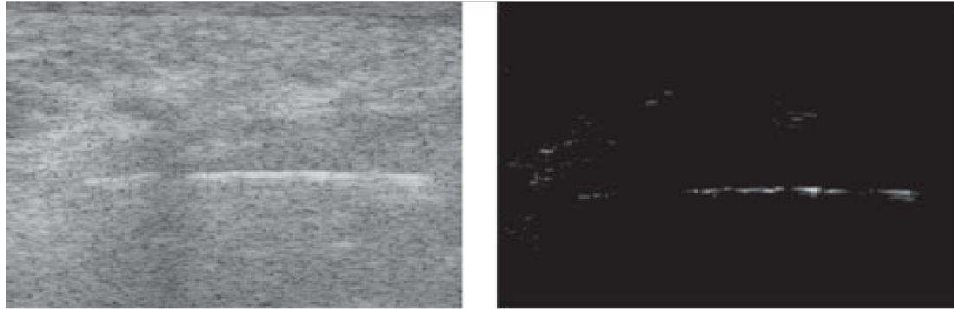
Figure 2.1: A comparison of a Reflected Power image (left) and a B-mode image (right) used to detect seeds in ultrasound images of a patient. This image is taken from published work by Moradi *et al.* [48]

can be viewed with respect to the anatomy (see Chapter 4, Section 4.2.5).

The seed reconstruction algorithm is applied to TRUS volumes that were acquired immediately after the seeds were implanted into a patient. The seed positions are calculated by computing a Reflected Power (RP) image from raw Radio Frequency (RF) data (see Figure 2.1) before applying template matching to find the seeds [80]. The reconstruction process takes ∼13 ms per 2D frame [48] which is fast enough for use in intra-operative planning. A complete volume sweep is obtained by collecting 270 frames from rotation angles of - 45 ^{o} to + 50 ^{o} at 21 frames per second so the total acquisition time is ∼15 seconds. The TRUS robot used to roll the TRUS probe is described in Section 5.5.

2.3 Method for Seed Localization in Fluoro

Research dating back to the early 1980s has shown that it is possible to reconstruct the 3D position of a seed using 3 fluoroscopic images [4, 5, 13, 62]. Since then several improvements have been made by incorporating C-arm calibration and correcting for errors in the C-arm pose [16] which allow for accurate reconstruction of the complete seed cloud. For this study a GE Series 9800 mobile C-arm was used to acquire 5 images at angles ranging from $-10°$ to $+10°$ for each patient. The exact angle of rotation was measured using a digital protractor. The data was collected after all the needles were inserted so that the standard procedure was not interrupted. However, the methods used for reconstruction can be used at any time
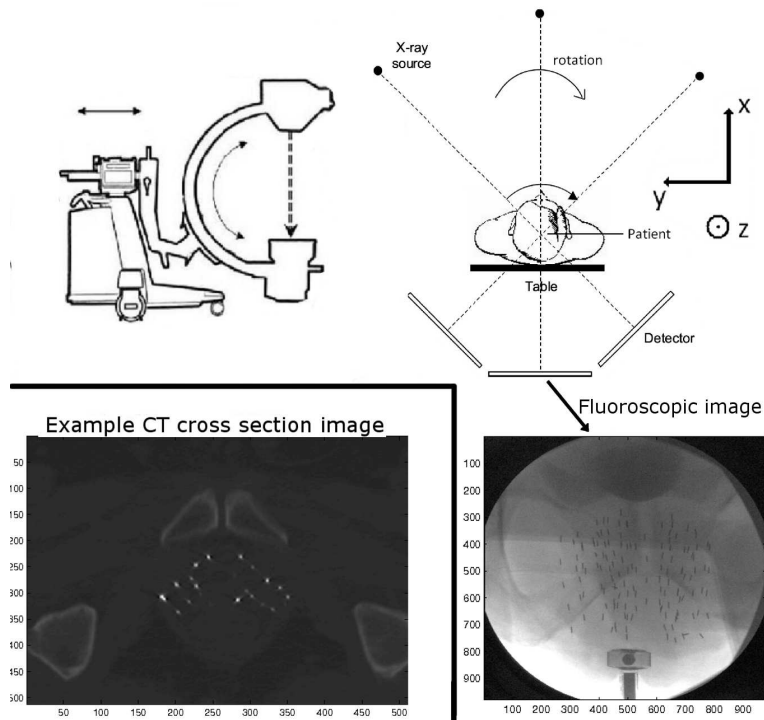
Figure 2.2: The use of a C-arm in prostate brachytherapy to obtain intra-operative fluoroscopic data. The coordinate system that is used in this document is also shown. Inset: An example 2D CT cross section image for comparison.

in the middle of a procedure - when there are still more needles to insert - as would be done with intra-operative planning. Figure 2.2 shows the setup used to get the fluoro data.

The main steps required for intra-operative seed reconstruction from fluoro are:

1. Segment the brachytherapy seeds in each fluoro image.

2. "Back-project" the segmented seeds to compute the 3D locations.

3. Repeat the process in an iterative manner using the computed reconstruction to correct for C-arm motion each time.

Each of these steps will be described in the following subsections.

2.3.1 Real-Time Seed Segmentation in Fluoro Images

Segmenting a fluoro image involves creating a binary image by assigning a value of 1 (or TRUE) to all pixels that are part of a seed and a value of 0 (or FALSE) to all pixels that are not. Figure 2.4 shows how a fully segmented image can be created from a raw fluoro image.

The presence of a seed is determined by thresholding: a local maximum and average is computed in a small window around each pixel to assign a cut-off that determines whether it is a seed pixel or not. A majority of the processing is done in Matlab (Mathworks, Natick, MA) which has several useful image processing tools. However, this algorithm requires large nested loops to move the small window through the entire image which takes ∼30 seconds per image when using pure Matlab code. This would make it very inconvenient to use intra-operatively and so required optimization. To speed the process up, the nested loops were re-written in C and re-compiled to be used as Matlab functions using the Matlab "mex" function. This change allowed the code to run up to 40 times faster making it suitable for use in the OR. Note that it is assumed that there is a method of retrieving the images directly onto an external computer once they are acquired.

Although the small window used to compute local thresholds works well to detect seeds, it also detects false positive seed pixels in large uniform regions (greater than the size of the window) or at sharp boundaries. In Figure 2.3, false positive seed pixels that are found outside the detector circle and around the probe can be seen. To solve this, either manual or automatic selection of a Region of Interest (ROI) that removes the probe and detector edge from the image, is needed. Note that the image of the probe would obscure the seeds if it was left fully inserted. Therefore, the probe is retracted during fluoro image acquisition to allow the complete seed cluster to be visible. This creates problems when trying to register fluoro and ultrasound datasets since the prostate deforms when compressed by the TRUS probe and returns to its original shape when the probe is retracted. This issue has been addressed by Moradi et al. [48](see Section 4.2.5).

12
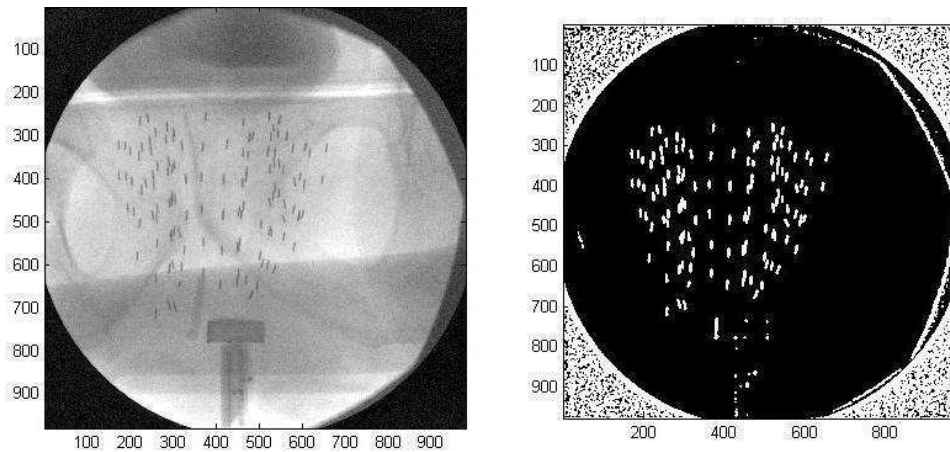
Figure 2.3: False positive seed pixels (white) found outside the detector circle in a segmented image (right). The unsegmented image (left) is also shown.
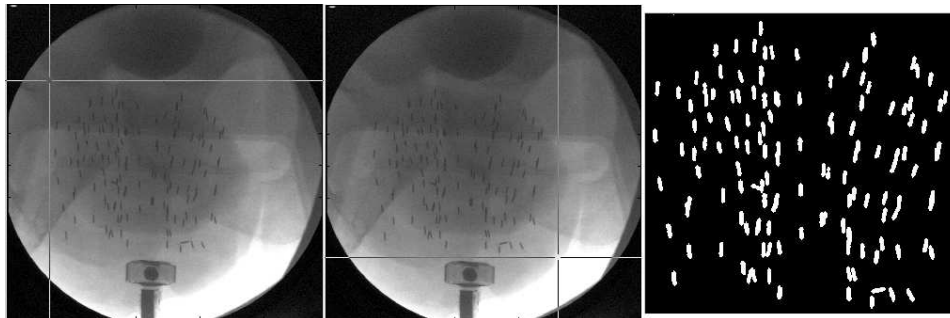
Figure 2.4: Manual selection of a ROI to select a "seed only" region. The top-left corner is first selected (left), followed by the bottom right to define the ROI used to produce a truly segmented image.

Manual ROI Selection

A ROI that does not include the ultrasound transducer (or probe) or the detector edge can easily be defined manually. The user can use a mouse click to select the top-left corner followed by the bottom-right corner of a rectangular "seed only" region. This process, shown in Figure 2.4, produces a truly segmented image.

This works well to produce consistent segmented images but may be inconvenient in the OR especially when it has to be done for 5 images. It is worth while

13
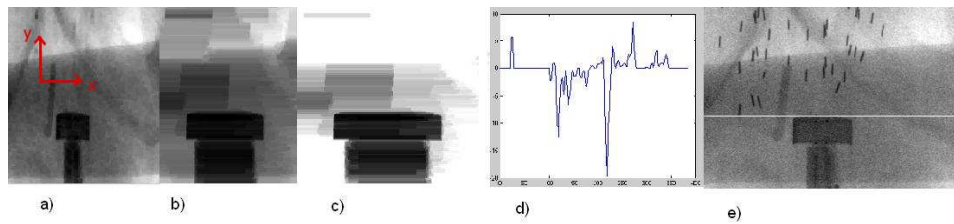
Figure 2.5: The full probe tip detection algorithm: a) The original image (with the coordinate system used), b) horizontal blurring, c) contrast adjustment d) gradient of the y-projection e) final image with horizontal line defining the bottom of the ROI.

therefore to consider methods to automate the selection of a ROI.

Automatic ROI Selection

There are two main components that need to be considered for identifying a seed only region. Firstly, it must be inside the detector edge. There is no image outside this circle and the local threshold algorithm does not work here. Secondly, it must remove the ultrasound probe from the image which has regions of sharp contrast that can be mistaken for seeds. The first part is fairly trivial since the detector edge is always in the same place in the image and can just be masked out. It is more complicated, however, to remove the probe from the image since its location varies between images and patients.

The approach taken is to find a horizontal line that is tangent to the tip of the probe and select the region above this as the seed only region. A series of image processing is performed including horizontal blurring and contrast adjustment before the gradient of the y-projection is used to find the probe tip. Figure 2.5 shows all the intermediary stages for the probe tip detection algorithm, with the coordinate system used, and Figure 2.6 shows the complete automatic segmentation process.

With the presented algorithms, the seed segmentation process can be performed automatically and quickly for all 5 images which makes it more feasible to use fluoro data to obtain seed positions for intra-operative planning.
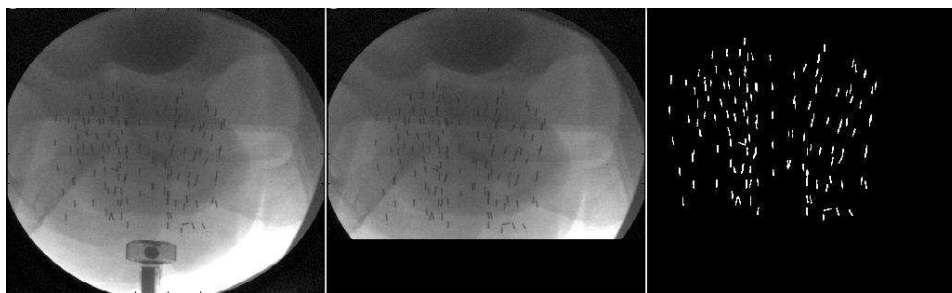
Figure 2.6: The complete automatic seed segmentation process. The seeds are segmented from the original image (left) by first finding the transducer tip (middle) and then thresholding the seeds.
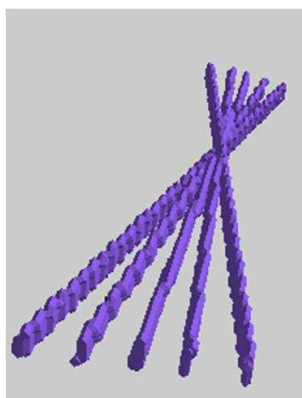
Figure 2.7: An illustration of the 5 backprojected lines for a single seed intersecting at the original 3D location of the seed.

2.4   Backprojection Algorithm and User Interface (UI)

Once the segmented images are obtained they can be used to reconstruct the 3D positions of the seeds since the angles of acquisition as well as the detector and source locations are known. Rays originating from seed pixels in a given segmented image can be *back-projected* to the source from the location of the detector. This can be done for each of the 5 segmented images and will create intersections in a 3D volume where the seeds would have been. Figure 2.7 shows the 5 back-projected seed pixel groups for a single seed intersecting at a point.

A Graphical User Interface (GUI) was developed in C++ that incorporated the
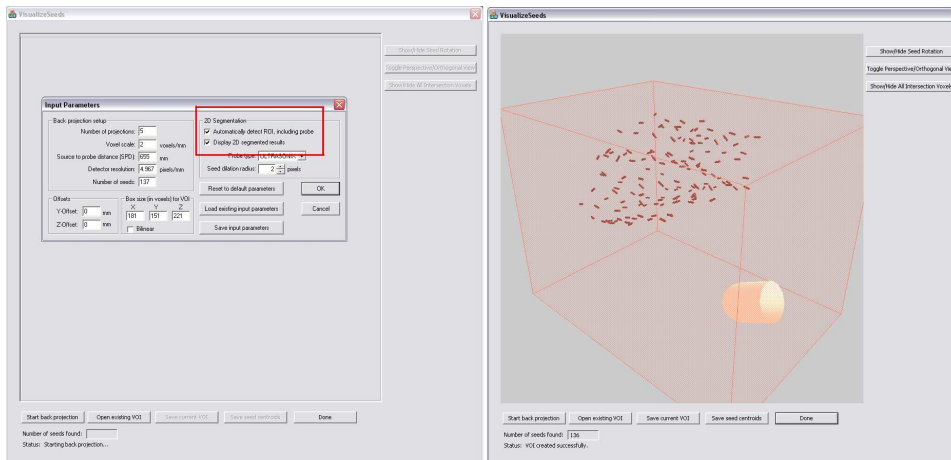
Figure 2.8: The GUI used for 3D reconstruction of seed positions from intra-operative fluoro data. On the left, the red box shows the options for manual and automatic segmentation as well as suppressing the segmented image display. The final result is displayed on the right.

segmentation and back-projection algorithms to reconstruct the seed positions and display the results in real time. The seed coordinates are taken to be at the centroid of a voxel cluster that is formed at an intersection. Seed shaped cylinders are then displayed at these locations. Figure 2.8 shows the GUI layout. Options for both manual and automatic segmentation are provided. This kind of visualization would be useful to look at seed distributions inside the OR.

To summarize the above sections, a GUI was developed that can automatically or manually segment fluoro images and then reconstruct the 3D positions of the seeds in real time. The backprojection algorithm used, however, does not take into account errors in the C-arm position due to oscillation or sagging of the source downward, which greatly reduces the quality of the reconstruction. A different method must be used to compensate for such motion.

2.5 C-arm Motion Compensation and Seed Matching for Robust Reconstruction

Dehghan *et al.* presented a method of compensating for C-arm motion by using the reconstructed seed positions to improve C-arm pose estimates iteratively [16].

This algorithm still requires a complete, though potentially incorrect, reconstruction of the seeds which cannot be done using the back projection method which relies on complete intersections to find the seed positions. Instead, a symbolic intersection is found, which is the point that achieves the minimum distance between back projected lines. Seed matching is done by minimizing this distance for all the projections for every seed. A suitably fast and accurate method called XMARSHAL has been developed by Kon *et al.* to do this while also taking into account hidden seeds in the segmented images [37]. These methods are not currently part of the current GUI but can replace the backprojection code following the automatic segmentation to provide real-time seed localization from fluoro data.

Seed displacement calculations and registration of fluoro to ultrasound, described in Chapter 4, both rely heavily on accurate seed reconstruction from fluoro data. The automatic segmentation algorithm, combined with fast and accurate matching, as well as C-arm motion compensation provide this. Accurate seed cloud reconstructions, performed by Dehghan *et al.*, from the patient study described in Section 2.1 are used in this thesis. The reconstructed seed positions have a localization error of less than 0.9 mm [17] and are computed in under 20 seconds per patient [17]. This accuracy and speed of this process makes it suitable for intra-operative planning.

Chapter 3

Simplifying Dataset Representation Using Needle Track Detection

3.1 Introduction

The measurement of seed displacements and the registration of fluoro to ultrasound (see Chapter 4) both require an in depth analysis of the seed cloud reconstructions from Chapter 2. Referring back to Table 2.1, a wide range of datasets exist for the seed reconstruction which are all required for intra-operative planning. Seed matching is required between all the datasets which can have up to 150 seed positions in each. This chapter describes a method of simplifying the representation of the seed clusters to make the seed matching process easier.

The seed matching problem can be very complex when dealing with so many cluttered points in several datasets. However, incorporating information about any known spacial relationships between the seeds can drastically reduce the complexity of the matching problem. During a standard brachytherapy procedure, the radioactive seeds are deposited in groups using needles. With this knowledge, it seems intuitive to group seeds into their corresponding needle tracks so that the matching problem is then reduced to matching $\sim$25 needle groups instead of $\sim$150

seeds. The methods presented in this chapter describe a new algorithm used to assign seeds to their corresponding needle tracks.

There are actually two main implant types used: Suture-embedded or *stranded* implants (RAPIDStrand; Oncura, Plymouth Meeting, PA) and *loose* seeds delivered using the Mick applicator (Mick Nuclear, Bronx, NY). However, studies have shown that stranded seeds provide better dose coverage[20] and less seed loss[60] without compromising the biochemical No Evidence of Disease (bNED)[28] - bNED is defined as having a sufficiently low Prostate-Specific Antigen (PSA) level for a period of greater than one year. Indeed, stranded seeds are used in about 50% of cases in the United States and in over 80% of cases around the world. There is therefore an incentive to focus seed matching methods on stranded seeds. Doing so takes advantage of the fact the the seeds are more physically constrained in stranded implants allowing tighter, more robust restrictions for seed spacing when detecting needle tracks. It should be noted that the methods presented in this thesis are still applicaple, with fewer contraints, to loose seeds since they are usually inserted in needles and evenly spaced.

In Chng *et al.*, seeds segmented from CT data were automatically grouped into their respective needle tracks using a minimum cost network flow algorithm [3, 14] following a coarse registration performed by iterating through all trajectory angles of every seed. The cost function consisted of complex correspondence functions used to compute the positional error, trajectory angle error and the strand spacing error [15]. This algorithm worked well to detect needle tracks in post-implant datasets. This chapter describes a method of extending this approach to work with intra-operative fluoro data as well as post-implant and pre-plan data by simplifying the cost functions used and making use of a different coarse registration algorithm.

3.2   Methods

The datasets were simplified by grouping seeds into their corresponding needle tracks. This makes the seed matching problem needed for seed displacement calculation and registration of fluoro to ultrasound easier. The following sections explain the methods used to perform the needle grouping.
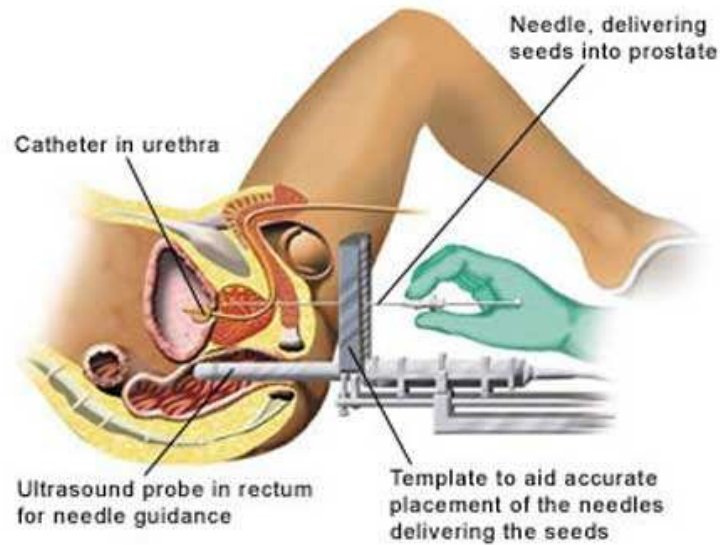
Figure 3.1: An illustration of the brachytherapy procedure. A square face needle guide template used to guide needle insertion. (This images was taken from www.roboticprostatecentre.co.uk)

3.2.1 Orientation of the Datasets to Allow Fine Tuned Needle Searching

In order to use a needle track detection algorithm on all the datasets it is necessary to first rotate each dataset into a recognizable orientation. In other words, the dataset must be rotated so that all the needle tracks are in the same general direction which makes it easier to then search for the strands.

In a standard brachytherapy procedure, needles are inserted through a square-faced needle guide template (see Figure 3.1). This creates a general direction of insertion, perpendicular to the square-faced template, that will be referred to as the *implantation axis*. Excluding the pre-plan dataset where all the seeds are in pre-defined tracks parallel to the z axis by design (see Figure 2.2 for the coordinate system used), the implantation axis is different for each dataset and does not line up with any axis. This is because the reconstructions in fluoro and CT are done with respect to their own coordinate systems independent of the implantation axis. Orienting of the datasets to allow the needle tracks to be detected can done by

finding the implantation axis in each dataset and then rotating the entire cluster so that the implantation axis is parallel to the z axis. This means the tracks can be found by searching for lines or curves that are in the same general direction as the z axis. With this method, detection of the implantation axis for the fluoro and CT data can be done independently without having to perform a rigid point set registration to the pre-plan which has been done by Chng *et al.* [15].

For the implantation axis detection, an "iterative best line detection" algorithm is used to obtain a ranked list of potential needle tracks in images. This algorithm is similar to the RANdom Sample Consensus (RANSAC) [22] algorithm which involves fitting lines to pairs of randomly chosen points and scoring each line until a threshold score is reached.

The algorithm steps are described below:

1. Select a pair of seeds to define a straight line.

2. If the angle between the line and the z axis is greater than a pre-defined threshold angle then reject it and return to step 1. Otherwise go to step 3.

3. Compute a *score* for the line based on a set of cost functions that take into account information on what needle tracks are expected to look like. Return to step 1 until all possible pairs of points have been chosen.

4. Rank each line according to the score and pick the top 8 lines to determine the implantation axis.

Since it is not computationally demanding to extensively search through all pairs of points, it is not necessary to randomly pick pairs of points. A full ranked list of all possible lines is instead created. For example, for 150 seeds, $\binom{150}{2} = 11175$ pairs of points can be defined and a majority of these would be deemed implausible at step 2 of the algorithm saving unnecessary calculations. Therefore it is acceptable to search all possible pairs of points.

The cost functions used in step 3 are tuned to find needle tracks. The total score for a potential needle track is computed by summing the contributions of all the seeds that fall within a Gaussian cone and are appropriately spaced:
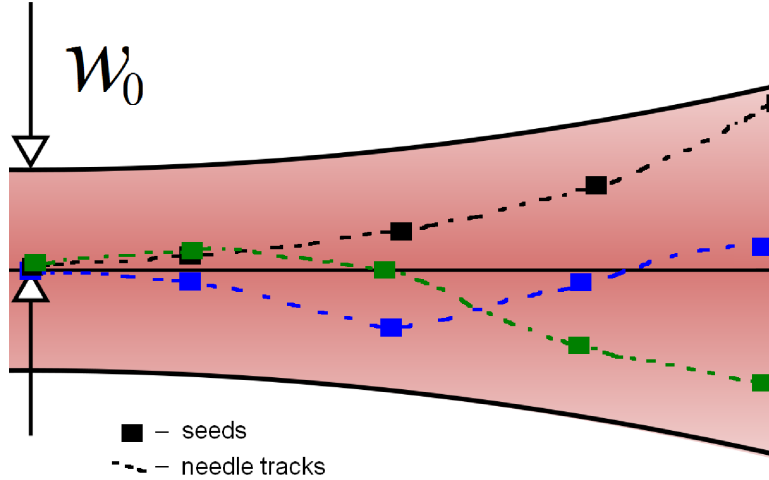
Figure 3.2: A Gaussian tolerance region used to score a potential needle track. Several possible needle track curvatures are shown.

$$Score = \sum_{\{i: d_i < w_i, |sp_{ij}-10| < 2 \forall j\}} e^{\frac{-d_i^2}{w_i^2}} \tag{3.1}$$

Here, d_i is the distance of seed i from the potential needle axis and sp_{ij} is the spacing between seed i and an adjacent seed j. The exponential component favours seeds that are closer to the potential line so that straighter lines are ranked higher so that the implantation axis is not affected by extremely curved needle tracks. The conditions beneath the summation define the components of the cost function.

The first component of the cost function ($d_i < w_i$) takes into account the number of seeds that fall within a certain threshold radius w_i from the defined line. A fixed threshold radius cannot be used since the needle tracks can exhibit significant curvature which varies from track to track. Instead a Gaussian cone is used to define a tolerance region for the line which is being scored, as seen in Figure 3.2.

Any seed that falls within the tolerance region contributes towards the score of the potential track. The radius or "waist", w, of the Gaussian cone expands in-

creasingly with distance, a, from the insertion plane. The insertion plane is defined as the z location of the most inferior seed (the seed closest to the perineum once inserted). A Gaussian cone was chosen for the tolerance region since it is useful to be able to tune both the waist and the rate of expansion of the cone to find the needle tracks. The curved surface of the Gaussian cone make it possible to keep a sharper cut-off at further distances while still having a relatively large final waist (at the farthest point from the insertion plane). The waist, w_i for a given seed, i, depends on the distance, a_i, of the seed from the insertion plane:

$$w_i = w_0 \sqrt{1 + \frac{a_i}{r}} \tag{3.2}$$

w_0 is the minimum waist size and r is the distance at which $w_i = w_0 \sqrt{2}$. These two parameters are used to control the minimum waist (at the insertion plane) and the rate of expansion of the Gaussian tolerance cone.

The second component of the score ($|sp_{ij} - 10| < 2 \forall j$) takes into account knowledge of the expected spacing between the seeds. For stranded implants especially, the seeds can only be a multiple of 10 mm from each other. Seeds must therefore fall within the Gaussian cone and also satisfy the spacing requirement with a tolerance of ± 2 mm to be counted in the score. This eliminates the cases when seeds from other needle tracks fall within the Gaussian cone.

As shown in section 3.3.1, the iterative best line detection algorithm correctly assigns a majority of the seeds to their corresponding needle tracks. However, a higher accuracy is needed to allow the possibility of intra-operative planning. The methods fails to assign all the seeds in most cases mainly due to the large variation in the curvatures of the different tracks which cannot be fully accounted for using a line fitting method. Still, since the seed assignment is still accurate for the highest ranked needles, averaging their directions does consistently find the implantation axis in both the fluoro and the CT datasets. The top 8 needles were chosen to keep the number consistent between datasets. Once the datasets are rotated to align the implantation axis to the z axis, a network flow algorithm that is not affected by the existence of intense curvature in the lines is used.
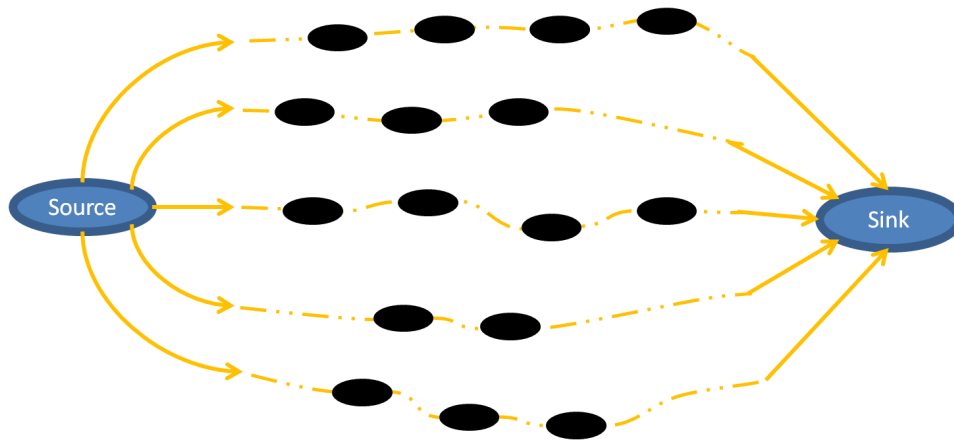
Figure 3.3: A simplified flow network with a source producing 5 flow lines that must flow though a cluster of transshipment nodes to a sink node.

3.2.2 Minimum Cost Network Flow Algorithm for Needle Track Detection

Rotating the datasets to align the implantation axis with the z axis simplifies needle detection process by reducing the search angle needed to find tracks. However, the tracks are still severely curved in some cases and cannot be parametrized. Therefore, the problem is changed from a line detection problem to a network flow system. Each seed is considered a node that can transfer a single unit of "flow" through it. Thus, they will be referred to as "transshipment" nodes. A single "source" node is created that feeds N flow lines into the system along with a "sink" node which receives them. The problem is then solved by finding the most efficient way for the flow lines to go from the source to the sink through all the transshipment nodes. Figure 3.3 illustrates a simplified version of the network flow system where $N=5$. This problem is analogous to finding the most efficient design for a water pipe system with a single provider feeding several units. For the case of the needle track detection problem, the N flow lines correspond to the number of needles inserted.

In order to find a most efficient network, the cost of a every potential connection between two nodes must be computed. The costs are computed as follows:

1. Each transshipment node (or seed) is assigned the same cost so that they are

each equally likely to be used.

2. For a given node, the costs of making connections to every other node are computed using a function that favours well spaced nodes that are in a reasonable direction.

3. Step 2 is repeated for every node so that each node has a list of costs for each connection it can make.

Since each arc or connection is independent of the previous one, there are no restrictions as to the direction of the flow based on the shape of the curve before the node. This allows for the sudden changes in direction that sometimes occur. The function used to compute the costs in Step 2 has two components that are similar to the ones defined in Section 3.2.1. The first component penalizes flow lines that deviate from that direction of the implantation axis. The angle cost, AC_{ij}, between two nodes i and j is computed as:

$$AC_{ij} = (e^{|\theta_{ij}|/\theta_0} - 1)^4 \tag{3.3}$$

where θ_{ij} is the angle from the implantation axis and θ_0 is a parameter used to tune how strict the function is. A higher value of θ_0 increases the acceptable range of angles. The 4th power for the angle cost ensures that the cost increases rapidly for increasing angles.

The second component of the cost function favours nodes or seeds that are multiples of 10 mm apart, as is expected for needle implants and especially for stranded implants. Higher multiples of 10 mm becomes increasingly unlikely these are considered less efficient in the flow network. The spacing cost, SC_{ij}, is defined as:

$$SC_{ij} = -e^{-s_{ij}/s_d}((\sum_n \delta(s_{ij} - ns_0)) \star e^{-(s_{ij}/s_v)^2}) \tag{3.4}$$

where s_{ij} is the spacing between node i and node j and $|\theta_{ij}|$ is the absolute value of angle the line between the two nodes makes with the z axis. The spacing cost is defined as a Gaussian peak with a variance of s_v. The symbol $\star$ denotes convolution which is just used to reproduce the function at integer multiples of 10
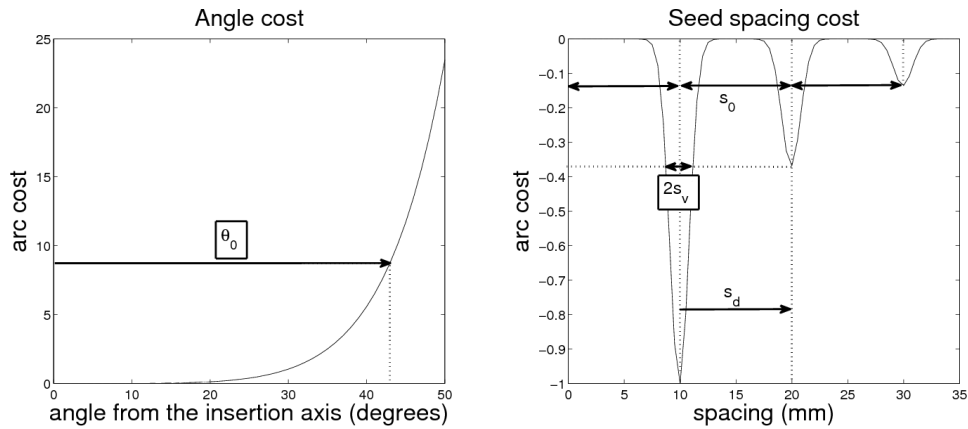
Figure 3.4: Graphs of the angle (left) and spacing (right) components of the cost function. Connections with smaller angles and acceptable spacing (multiples of 10 mm) are favoured. The tunable parameters for the angle variance, θ_0, and the spacing tolerance, s_v, are shown with a box around them. The spacing constants, s_0 and s_d are also shown.

($s_0 = 10$ *mm*) using a train of delta functions. The decaying exponential with a variance of $s_d = 10$ *mm* is aimed at penalizing larger seed spacing. It decreases the magnitude of the spacing cost by a factor $1/e$ for every successive integer multiple of the spacing s_0. Note that the contribution of each successive Gaussian peak to the cost decreases exponentially as *n* increases. However, in practice, it is extremely unlikely that the seed spacing in a given needle is 40 mm or more so the sum was only done until $n = 3$. s_v is another tunable parameter used to set the deviation allowed for the spacing.

Figure 3.4 graphically shows the angle and seed spacing cost functions with the different parameters and constants. Complex forms of these components are derived in Chng *et al.* [15]. The simplification of the functions allows the algorithm to easily be re-tuned for seed clusters reconstructed from different imaging modalities.

For the fluoro data, θ_0 was set to 43.0 degrees and s_v to 1.2 mm. A large angle variance was needed since several needle tracks were visibly curved and rotated but tighter restrictions on the seed separation ensured that true tracks were identified.

26

In contrast, for the post-implant CT data, θ_0 was set to 31.5 degrees and s_v to 3 mm. Here, the seeds migrated a little so the seed separation requirement was relaxed. In both cases the same parameters were used for all the patients.

A final tuning parameter, γ is used to weight which of the two components affects the total cost most. The total cost is obtained by summing the two costs with a weighting parameter, γ, on the angle cost term. This parameter controls which component affects the cost most. For the intra-operative fluoro and post-implant CT data, γ was set to 0.3. This increased the sensitivity to the spacing of the seeds and relaxed the dependence on the angle which was necessary to allow for the large changes in direction seen these datasets. For pre-plan data, the seeds are defined along tracks that are parallel to the implantation axis. Any deviation from this axis is therefore penalized and the cost is heavily weighted to the angle component (γ is set to 1.2). The final objective function is:

$$C_{ij} = \gamma AC_{ij} + SC_{ij} \tag{3.5}$$

The Matlab Toolbox "MATLOG" developed by Kay *et al.* is used to perform the minimization after the costs are computed [34] (North Carolina State University, Raleigh, NC; http://www.ise.ncsu.edu/kay/matlog/).

It is possible to define N, the number of needles inserted, before the computation. However, this may be tedious or inconvenient during a brachytherapy procedure. Here, the number of needles that have been inserted varies depending on when the oncologist wants to check the placement. Therefore, the algorithm is made to automatically compute the number of needles inserted. This is done by setting an arbitrarily high number of "flow lines" initially which results in several connections directly between the source and the sink without going through any seed nodes. The number of needles can then be reduced to the number flow lines that contain at least two seed nodes (the minimum number in a given needle) and then the whole process is repeated until only flow lines with at least two seed nodes are found.

Table 3.1: Needle track detection using the iterative best line detection algorithm.

Patient	Number of incorrectly assigned seeds	Number of seeds inserted	Percent seeds correctly assigned
1	21	105	80%
2	14	105	86.67%
3	16	102	84.31%
4	25	122	79.51%
5	8	104	92.31%
6	13	115	88.70%
7	21	100	79%
8	8	118	93.22%

3.3 Results

This section presents the results of the needle track detection algorithm for 8 patients. The implantation axis detection results are presented first, followed by the needle track detection results.

3.3.1 Implantation Axis Detection Results

The iterative best line detection algorithm was first validated by testing its ability to assign seeds to needle groups. The results, reported in Table 3.1, show that 79.0% to 93.22% of seeds that were correctly assigned. Figure 3.7 (appended at the end of this chapter) shows the results for patient 4 which produced a relatively low percentage assignment of 79.51%.

The implantation axis was found by averaging the vector directions of the eight highest scoring needles. The datasets were then rotated so that the implantation axis was aligned with the z axis. Figure 3.5 shows this alignment for both intra-operative fluoroscopic data and post-implant CT data. Although Figure 3.5 only shows the sagittal view, it is worth noting that the algorithm performed 3D rotations and not just a single rotation about the y axis.
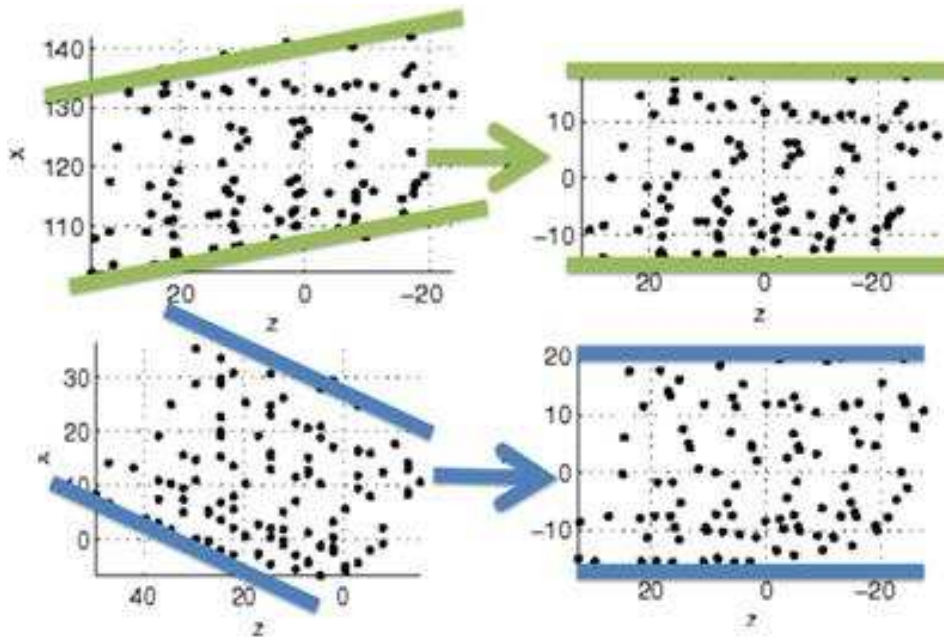
Figure 3.5: Finding the implantation axis using an iterative best line detection for intra-operative fluoro data (top) and post-implant CT data.

3.3.2 Needle Track Detection Results

The full algorithm was tested on 8 patient datasets. Figure 3.8 (appended at the end of this chapter) shows the results from a single patient for all three data types.

The total number of needles found as well as the correctness of the seed to needle assignments was checked by comparing the needle groups to the pre-plan. This was done by first comparing the intersections of detected needle lines at the insertion plane with those from the pre-plan, looking at the number of seeds per needle as well as the expected relative positions. This simplified the finding of potentially incorrectly assigned seeds. Figure 3.6 shows an example of a plan comparison. The black ellipses show how the comparison can be used to identify which seeds were not assigned correctly.

The needle matching for the pre-plan data, not surprisingly, correctly assigned all the seeds in all patients. The results for the intra-operative and post-implant seed
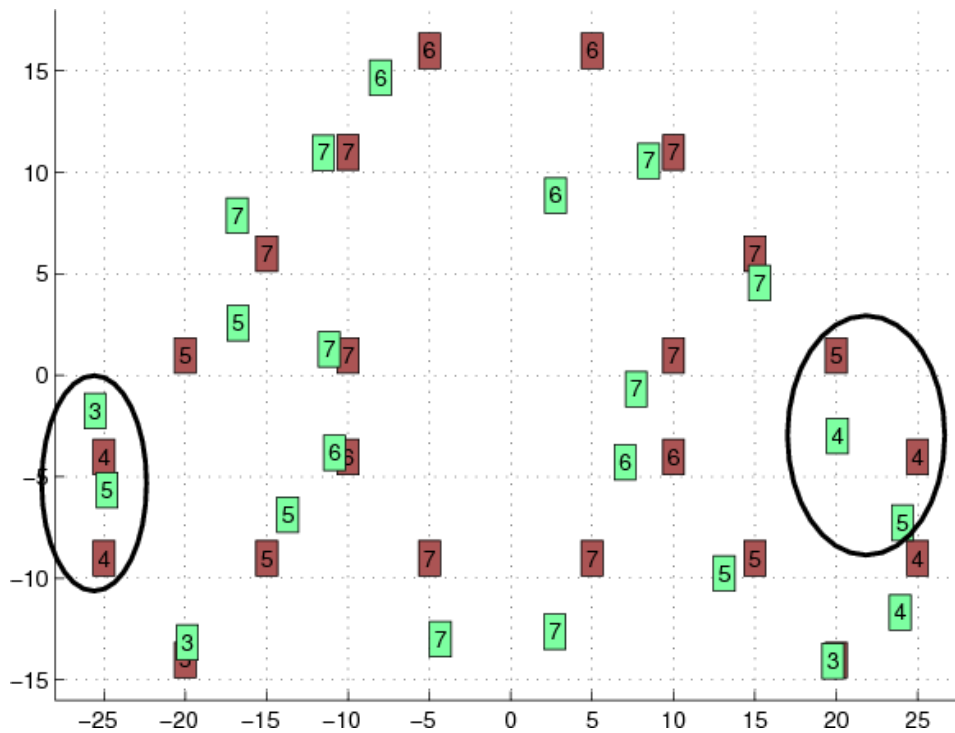
Figure 3.6: Comparison of fluoroscopic intersection data (green) with pre-plan data (red). The same images were used for CT to pre-plan comparison. The black ellipses show where there are incorrectly assigned seeds in the fluoro data.

to needle assignment are summarized in Table 3.2 which shows the percentage of seeds that were correctly assigned.

It is worthwhile to note that patients 3 and 5 had two special load needles (needles with irregular seed spacing) each. As expected, this made it more difficult to find those needles and accounted for the incorrect seed assignments for both these patients. However, the number of needles was correctly found 100% of the time for all types of data. Summarizing the needle assignment results, an average of 99.31% of the seeds were correctly assigned for the intra-operative data, while an average of 99.41% of the seeds were correctly assigned for the post-implant data. Once again, no pre-plan information is used in the needle detection and the

Table 3.2: Summary of needle track results for the both intra-operative and post-implant data, on 8 patients.

Patient	Number of seeds inserted	Percent intra-op seeds correctly assigned	Percent post-imp seeds correctly assigned
1	105	100%	100%
2	105	100%	98.10%
3*	102	98.04%	98.04%
4	122	98.36%	98.18%
5*	104	98.08%	100%
6	115	100%	100%
7	100	100%	100%
8	118	100%	100%

* patients with special load needles
(needles with irregular seed spacing)

algorithm takes between 1 to 2.5 seconds to rotate the cluster and find the needles.

3.4 Conclusion

Two techniques have been combined to formulate a method to group seeds into their corresponding needle tracks. The novelty of this method is its versatility in terms of the range of datasets it can be used for. The complete process involved: implantation axis detection, and needle track detection.

The iterative best line detection algorithm accurately found the implantation axis from rotated seed clusters in all the datasets. Detecting the implantation axis was used primarily to focus the search space required for the minimum cost network flow algorithm. However, this algorithm also plays a crucial role the registration of pre-plan, fluoro and CT datasets. This is described Section 4.2.1 in more detail.

With the detected implantation axis, seed assignment based on a minimum cost network flow algorithm has an accuracy of 99.3% and 99.4% in the intra-operative and post-operative data. The correct number of needles inserted was detected every time. The complete needle track detection algorithm has been shown to provide

fast, *automatic* and *reliable* seed grouping. All of these are necessary requirements for intra-operative planning.

The grouping of seeds into their corresponding needle tracks creates a simplified representation of the data. This reduces the complexity of the seed matching problem that is required for both seed displacement measurement and fluoro to ultrasound registration as described in Chapter 4.
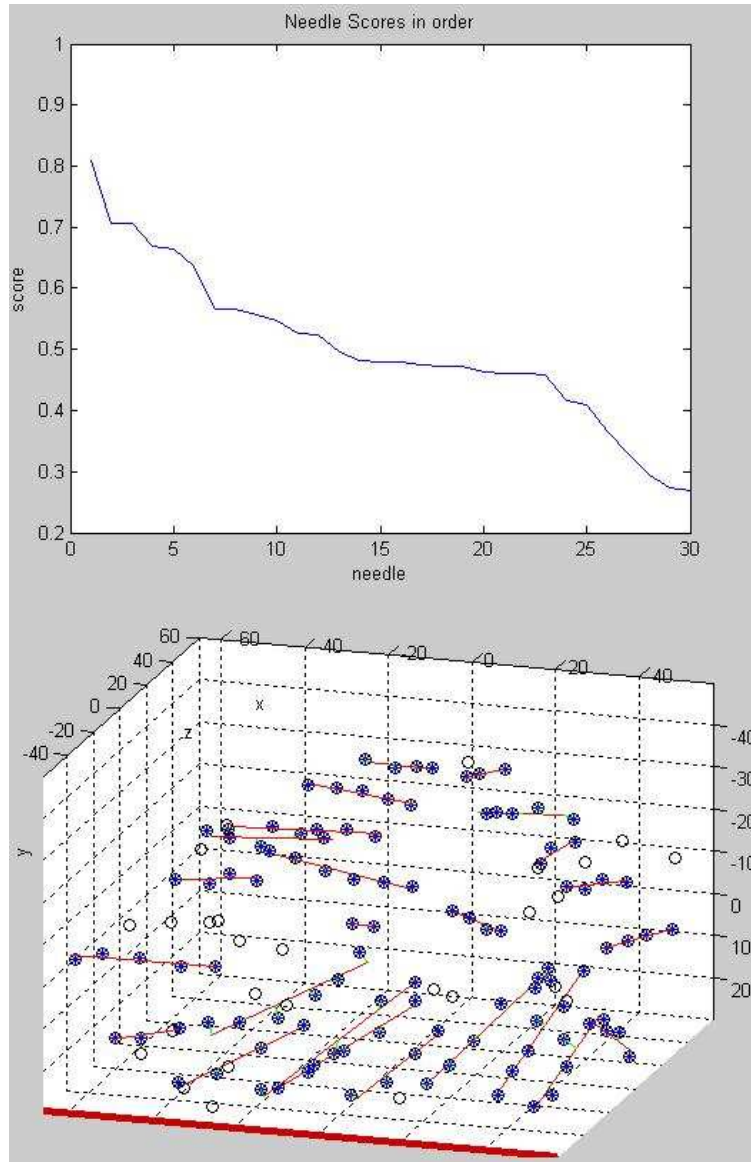
Figure 3.7: Using the iterative best line detection algorithm to rank possible needle tracks. The ordered needles are graphed above and an illustration of the best ranked needle tracks and the corresponding seed assignments is shown below.

Needle detection results from pre-plan data

Needle detection results from intra-operative fluoro data

Needle detection results from post-implant CT data
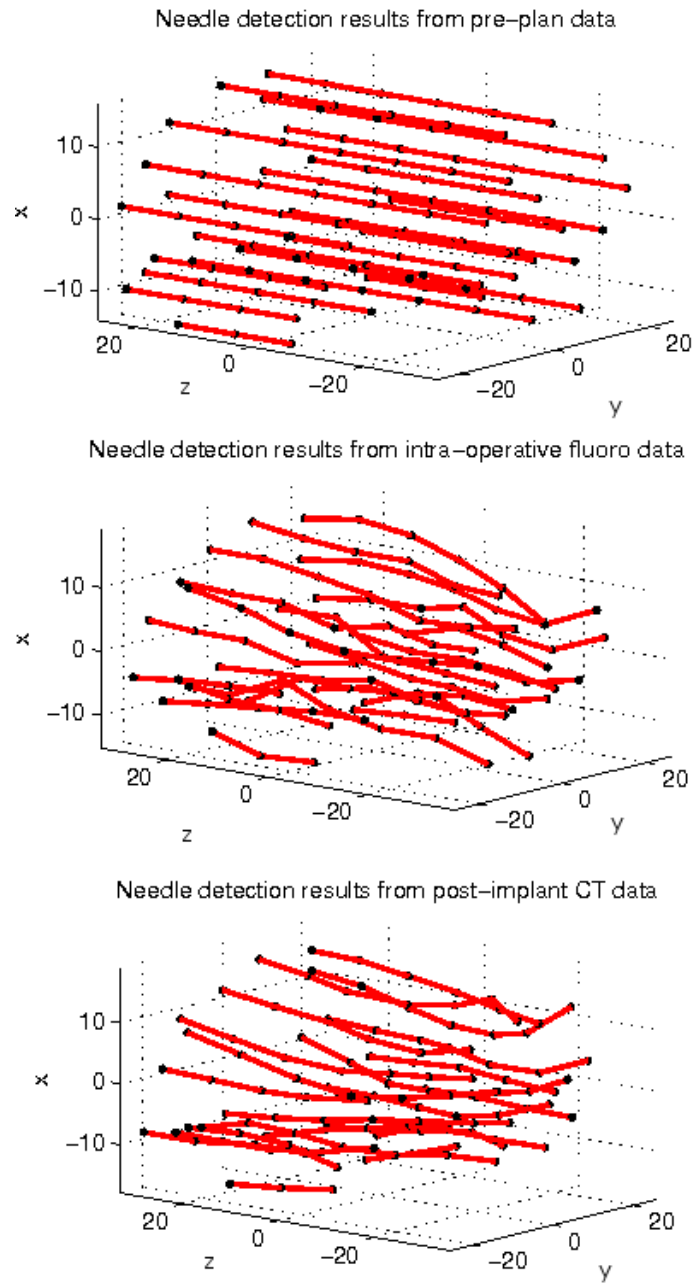
Figure 3.8: Needle track detection results for patient 4 for pre-plan, intra-operative and post-implant data

Chapter 4

Measuring Intra-operative and Post-implant Displacement of Seeds With Registration to Ultrasound Volumes

4.1 Introduction

This chapter describes how the needle track detection algorithm explained in Chapter 3 can be used to compute seed displacements and also to register these displacement values to an ultrasound volume. Measuring seed displacements with respect to the patient anatomy can be used to determine potential displacement trends or to allow intra-operative planning when used during an operation.

Several research groups have reported studies that involve measuring *post-implant* displacement of seeds. In most cases manual seed matching is used to compute seed migration [24, 33, 46, 61, 71]. It is more convenient, however, to have an automatic method of matching the seeds. This is true for pure post-implant dosimetry but is particularly important for intra-operative planning where there is not enough time to perform manual matching.

Pinkawa *et al.* investigated post-implant seed migration by looking at the dose

levels over a 30 day period instead of looking at individual seeds [57, 58]. This removed the need to match seeds in successive datasets but manual localization and contouring was still required which is not feasible in an intra-operative environment.

One method of automatically measuring the displacements is to monitor individual seed displacements relative to fiducials that are also inserted into the prostate. Usmani *et al.* performed a study using this idea, localizing seed positions relative to fiducial markers in repeated post-implant CT images [77]. Precise dose changes could be computed based on the seed positions but adding fiducials can be considered unnecessarily more invasive and errors can be created if the fiducials themselves migrate.

Other fully automatic methods for plan reconstruction [6, 15] for post-implant dosimetry have been studied. In Chng *et al.* a needle track detection algorithm, similar to the one in Chapter 3, was used to group the seeds. The "graphs" created by the needle track networks were then matched in successive post-implant CT images using a non-linear optimization algorithm called "Graduated Assignment" [15].

The use of post-operative data alone limits the conclusions that can be drawn. The migrations measured are caused mainly by post-implant inflammation of the prostate. Although it is valuable to know if any migration trends exist before an operation is performed, there are two other factors that could lead to seed displacement that need to be measured or known for intra-operative planning to work: *(i)* misplacement at the time of the implant and *(ii)* change in patient pose from dorsal lithotomy (see Figure 4.1) during the implant procedure to supine during CT imaging. In order measure these types of displacement, seed matching is needed with *intra-operative* data. The matching of seeds in pre-plan data to those from intra-operative data gives information on seed misplacement during an operation while the comparison of intra-operative to post-implant seed positions investigates movement due to change in patient pose.

Intra-operative dosimetry requires that any seed distributions or displacements be known with respect to the target volume. In order to analyze and potentially modify a plan intra-operatively, it is crucial to know what the effect of any displacements are in terms of coverage of the prostate and target regions. To do this,

Figure 4.1: A patient in a mock setup at the BC Cancer Agency illustrating dorsal lithotomy position.

the seed reconstructions must be registered to a dataset that can reliably see the soft tissue. The prostate and surrounding anatomical features are all visible in TRUS images which is currently used in standard brachytherapy operations making it an ideal imaging modality for this.

Research has been done to detect all the seeds using TRUS alone [27, 82], which would in itself allow intra-operative planning without the need for fluoro data, but even with manual segmentation, up to 25% of the seeds cannot be localized [27]. Therefore, TRUS to fluoro fusion is a suitable alternative.

Various methods of fluoro to ultrasound fusion have been tried [23, 48, 68, 75, 76]. One method could be to use Digitally Reconstructed Radiography (DRR) to simulate fluoro images of the TRUS probe using a pre-operative CT volume to determine its position relative to the seeds [65, 84]. This has yet to be tested for prostate brachytherapy. Another method is to use seed based registration by registering incomplete datasets from ultrasound data to complete datasets in fluoro [48, 68, 75, 76]. The main issue with this method is the dependence on a complete

reconstruction from the fluoro dataset. Moradi *et al.* present such a registration [48] using complete fluoro reconstructions with C-arm motion compensation [17]. In this process, the needle track detection algorithm makes it possible to match the detected seeds between the datasets so that they can be rigidly registered.

4.2 Methods

This section explains how the needle track detection algorithm described in Chapter 3 are used to match seeds in fluoro, CT, ultrasound, and pre-plan dataset to compute seed displacements with respect to the prostate. Sections 4.2.1, 4.2.2, 4.2.3 and 4.2.4 describe how the seed displacements are computed and Section 4.2.5 explains how the fluoro data can be registered to TRUS data so that the displacements can be known relative to patient anatomy.

4.2.1 Registration of the Pre-plan, Fluoro and CT Seed Clusters

Seed displacements are computed by looking at the difference in position of a given seed before, during and after an operation. To do these comparisons, the coordinates of the seeds in the different datasets must be defined with respect to the same set of axes and so the pre-plan, fluoro and CT seed clusters be registered.

Figure 4.2 summarizes the registration process that is used, which allows actual seed displacements to be measured. It starts by setting the origin of each dataset as the seed cluster centroid position. Usmani *et al.* show that the seed cluster centroid position can be used to register the datasets since it remains at the same position even with considerable post-implant migration[77]. This means that the centroid position is the same in all the datasets.

The next step takes advantage of the implantation axis detection algorithm described in Section 3.2.1. This algorithm aligns the implantation axis with the z axis to help with needle track detection. This alignment in effect also corrects for global rotations about the x and y axis which almost completely registers the datasets. Note that both the centroid computation and the implantation axis detection can be done on each dataset separately. The datasets can therefore be put into correspondence without having to do a rigid point set registration, using Iterative Closest Point (ICP) [11] for example, by comparing two full datasets.
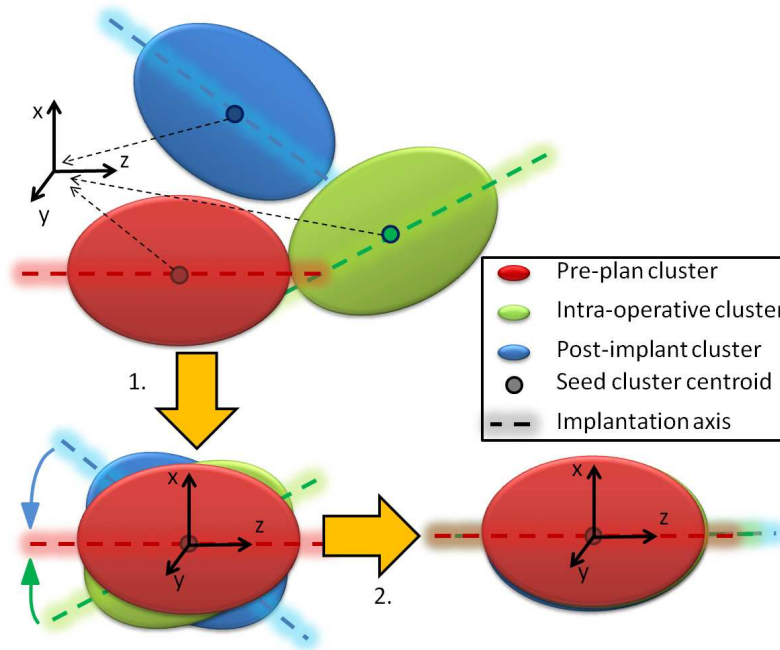
Figure 4.2: An illustration of the two-step global registration technique used.
Step 1. Compute the seed cluster centroid locations and move them to a
global origin. Step 2. Rotate each dataset so that the implantation axis
is aligned with the global z axis. Post-processing is used to correct for
roll offsets. Once all the datasets are put in the same coordinate system,
actual seed displacements can be measured.

Any offset rotations about the implantation axis (which is now also the z axis)
are not removed. This rotation, called the "roll", is corrected using post-processing
as explained in section 4.2.4.

4.2.2   Needle Matching

The reason the needle track detection algorithm described in Chapter 3 makes the
seed displacement computation more feasible is because it simplifies a matching
of up to 150 seeds to one of ~20 needles. This section explains how the needle
matching across datasets is carried out.

Chng *et al.* use a graph theory method called "Graduated Assignment" to

match entire networks in successive post-implant datasets [15]. A different method is presented here.

After rotating the seed clusters and grouping the seeds into needles, the intersection of each needle track with the *insertion plane* is computed. The insertion plane is the transverse plane passing through the most inferior seed (at the apex of the prostate). The needle intersections are then matched between two datasets using a network flow system. This network is different from the network described in Section 3.2.2. In this case, every node in one dataset is defined as a source node that feeds 1 unit of flow into the system. Similarly, every node in the other dataset is defined as a sink node that receives 1 unit of flow. The cost, MC_{ij}, of connecting a given source node, i, to a sink node, j, depends on the Euclidean distance, d_{ij}, between the two needle intersections *as well as* the the number of seeds that are in the needles, N_i and N_j:

$$MC_{ij} = d_{ij} + (N_i - N_j + 1)^4;$$ (4.1)

The term $N_i - N_j + 1$ has a 1 added to it so that even if the difference is only 1, it will be penalized heavily by the fourth power. The cost is therefore only low if the needle intersections are close to each other *and* they have the same number of seeds. Figure 4.3 demonstrates why it is necessary to include the number of seeds in the matching cost. The red lines show some of the correct matches that would not have been assigned if a simple closest-to match had been used.

4.2.3 Seed Displacement Computation

Each seed position is compared to its corresponding seed from a different data type to obtain a displacement vector. This can be done intra-operatively to detect any misplacements by comparing actual seed positions to planned seed positions at any given time during the procedure. It is also valuable to quantify the intra-operative misplacement or post-implant movement to see if any trends exist. In order to find potential trends, an in-depth study was carried out on the patient data acquired.

An complete list of all the displacement vectors from every seed in each patient was created and used to compute trends. Displacement vectors were calculated both for intra-operative misplacement and for post-implant movement.
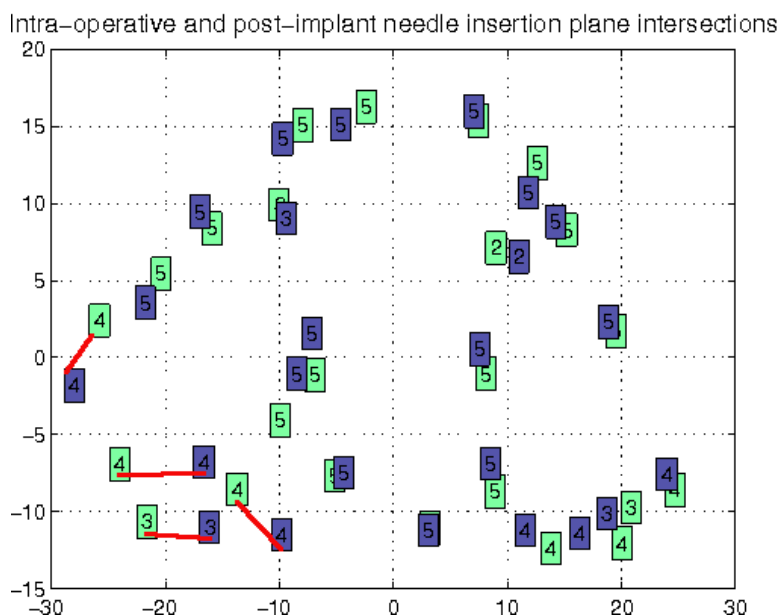
Figure 4.3: Intra-operative and post-implant insertion plane intersections for one patient. The red lines show situations where a purely closest-to match would not work without also taking into account the number of seeds per needle.

Scalar distances were used to quantify the absolute motion. The total average distance was computed for each patient as well as for all the patients. The average distance was also computed for different regions of the prostate by dividing the entire volume into 27 subregions, where each axis was divided into 3 sections.

Directional information was also recorded. This was done my computing an average displacement vector in each of the 27 subregions. These displacement vectors were used to analyze the trends in the direction of motion in each region.

4.2.4 Post-processing to Correct for Differences in Roll Between Datasets

In Section 4.2.1, the seed cluster centroid and the implantation axis are used to register pre-plan, fluoro and CT datasets. This corrects for all global differences except for differences in roll. A global offset is defined as one that is applied to
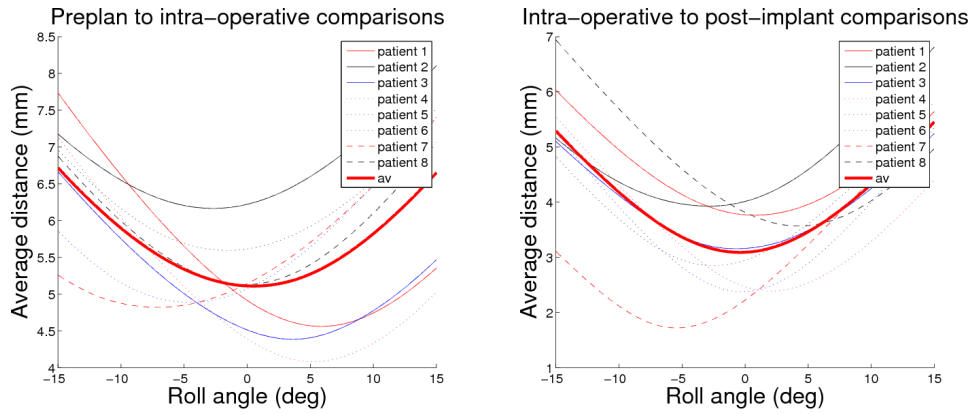
Figure 4.4: Graphs showing how the average displacement distances varied with different roll values for the intra-operative data. The pre-plan to intra-operative comparisons are shown on the left and intra-operative to post-implant comparisons are shown on the right.

the entire dataset rather than a small subregion. If there is a global roll offset between two datasets then all the computed local trends are influenced by it. In order to remove this offset an automatic post-processing method is used. The average displacement distance can be computed for each patient as in Section 4.2.3 for a range of different roll values for the intra-operative data. Figure 4.4 shows how the average displacement distance varied with roll angle for each patient. The intra-operative dataset is chosen since it is used in both comparisons. The roll angle which gives the lowest average displacement distance is taken to be the "no roll". This completes the registration process since all 6 global degrees of freedom are put into correspondence. The displacement results presented in Section 4.3.2 are roll offset corrected.

4.2.5   Registration of Fluoro to Ultrasound

The second objective of this thesis was to develop an algorithm to register fluoro datasets to ultrasound volumes. This is required to properly assess seed displacements for intra-operative planning. It allows changes in the seed distribution to be viewed with respect to the prostate and any other soft tissue features that are visible

in ultrasound.

The technique used to register the two volumes demonstrates another application for the needle track detection algorithm presented in Chapter 3. Here, the simplified "needle grouping" representation of the fluoro seed cluster is used to compare and match seeds to the ultrasound volume. The seeds act as fiducials since they are visible in both imaging modalities and this allows the fusion of the two.

Needle intersections are computed from the seed clusters reconstructed from fluoro data, as described in Section 4.2.2. Similarly, needle intersections with the insertion plane are computed for the ultrasound volumes using needle tracks found using the Hough transform [48, 80]. Registration is then performed by minimizing the following cost function:

$$Cost = \sum_{i}^{N_{US}} d_i \tag{4.2}$$

where N_{US} is the total number of ultrasound needle intersections and d_i is Euclidean distance to the nearest fluoro needle intersection from the ultrasound needle intersection i.

Since a complete ultrasound seed reconstruction dataset is rarely available, this alone is not enough to put the two datasets in full correspondence. However, it is still required to determine which fluoro seeds are also found in the ultrasound data so that rigid point set registration can be performed to fully register the two datasets.

Moradi *et al.* continue from this method using the ICP [11] method as well as a Gaussian Mixture Model (GMM) [32] to complete the registration process. In addition, the warping of the prostate when the TRUS is fully inserted as compared to when it is retracted to allow the seeds to be visible in the fluoro images is accounted for [7]. Validation of the needle matching and registration is done using a "leave-one-needle-out" method where all the seeds from needle group are removed to check if the results change [48]. If the results change significantly with the removal of a needle, it indicates the presence of a local minimum making the registration invalid.
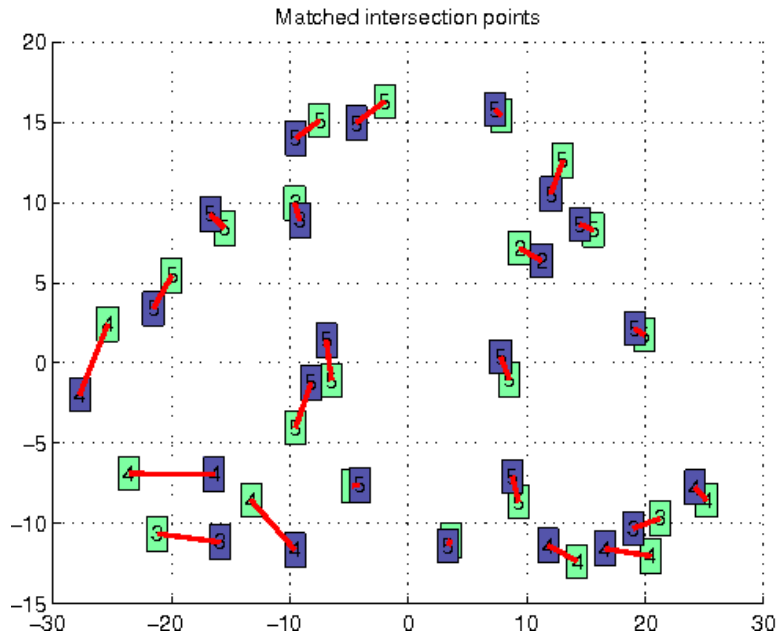
Figure 4.5: Intra-operative to post-implant needle matching results for one patient. Matching needles are connected with the red lines.

4.3 Patient Study Results

The patient study presented in this section was performed to verify if the methods described in Section 4.2 can be used to compute real-time seed misplacements with respect to the target volume to allow intra-operative planning. In addition, the various displacements are analyzed to determine possible trends in misplacement or movement which can help influence future plans. The results of a study on 8 patients are presented for inter-dataset needle matching and seed displacements. The seed displacements are divided into two types of displacement: intra-operative misplacement and post-implant movement.

4.3.1 Inter-Dataset Needle Matching

Figure 4.5 shows how the intersection data displayed in Figure 4.3 was correctly matched. The red lines connect needles that are matched by the algorithm. The needle track detection results presented in Section 3.3.2 show correct assignment
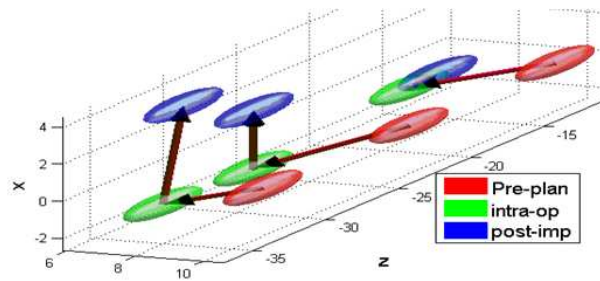
Figure 4.6: Displacements of seeds for a single needle. The intra-operative misplacement is seen from red to green and might be the kind of visualization that can be used in the OR for intra-operative planning.

for over 99% of the seeds. In order to fairly test the needle mathching algorithm, the few incorrectly assigned seeds in the various datasets were manually adjusted to be grouped with the correct needle. After this adjustment all the needles were correctly matched between all the datasets in under 2 seconds per patient using unoptimized Matlab code.

4.3.2 Seed Displacement Results

With the needles correctly identified and matched in corresponding data sets for a given patient, the seeds themselves could be directly compared to calculate seed displacements. The time taken to obtain the displacements once the seeds are matched is negligible since it merely a subtraction of 3D coordintates. Figure 4.10 (appended at the end of this chapter) shows the movements of the seeds between the pre-plan and intra-operative data and between the intra-operative and post-implant data for one of the patients. The usefulness of the displacement calculation for intra-operative planning is shown in Figure 4.6 which shows actual displacement results for all three sets of data for a single needle.

Average Displacement Magnitude Results

The three-dimensional Euclidean distance that every seed moved between datasets was computed. For each single patient the average distance was computed as the sum of all the distances moved divided by the total number of seeds inserted into

Table 4.1: Pre-plan to intra-operative and intra-operative to post-implant seed displacement results.

Patient	Av. misplacement distance (pre to intra-op) /mm	Av. movement distance (intra-op to post-imp) /mm
1	4.56±2.10	3.76±1.89
2	6.17±2.44	3.93±2.45
3	4.39±1.78	3.16±1.78
4	4.08±2.25	2.39±1.41
5	5.59±2.25	2.85±1.73
6	4.89±2.18	2.38±1.09
7	4.82±2.46	1.72±0.75
8	5.12±3.02	3.57±1.72
Average	4.94±2.42	2.97±1.81

the patient. The total average over all eight patients was also computed. Table 4.1 summarizes the results.

From Table 4.1 the average displacement was significantly larger for pre-plan to intra-operative case than intra-operative to post-implant data ($p < 0.01$, n= 871).

The error in localization of the seeds in intra-operative fluoroscopy data, is reported to be less than 0.9 mm [17]. The calculated displacement is therefore not due to errors in seed localization. The result suggests seed displacement due to oncologist preferences, needle deflection and prostate movement during needle insertion, seen from pre-plan to intra-operative misplacement as an average of 4.94 mm, is higher than displacement caused by a change in patient pose and immediate inflammation (measured as intra-operative to post-implant movement, an average of 2.97 mm).

Regional Displacement Magnitude Results

The average displacement was computed for each of the 27 subregions, defined by dividing each axis into 3 sections, to quantify the motion in each region. Tables 4.2 and 4.3 show these distances. In the table, the different transverse slices are

Table 4.2: Intra-operative seed misplacement results for different prostate regions

Average misplacement distance (mm)		left	mid y	right
	anterior	5.42 ± 1.41	6.52 ± 2.63	4.81 ± 2.41
inferior	mid x	4.11 ± 2.19	5.79 ± 2.41	4.01 ± 2.44
	posterior	4.25 ± 1.52	5.23 ± 1.76	4.16 ± 2.05
	anterior	5.13 ± 1.51	6.58 ± 3.07	5.38 ± 2.92
mid z	mid x	4.65 ± 2.14	6.15 ± 3.17	4.89 ± 2.36
	posterior	3.81 ± 1.68	5.07 ± 1.97	4.14 ± 2.88
	anterior	5.84 ± 1.25	6.70 ± 2.76	5.71 ± 2.09
superior	mid x	5.06 ± 2.20	5.55 ± 2.58	5.14 ± 2.51
	posterior	4.03 ± 1.93	5.24 ± 2.36	4.96 ± 3.01

Table 4.3: Post-implant seed movement results for different regions within the prostate volume

Average distance moved (mm)		left	mid y	right
	anterior	2.96 ± 1.71	3.67 ± 2.34	3.16 ± 1.81
inferior	mid x	2.99 ± 1.76	2.82 ± 1.57	3.34 ± 1.85
	posterior	2.66 ± 1.55	2.58 ± 1.60	3.26 ± 1.76
	anterior	2.68 ± 2.30	3.29 ± 2.45	3.13 ± 2.14
mid z	mid x	3.03 ± 2.01	1.60 ± 0.86	2.59 ± 1.90
	posterior	3.15 ± 1.42	2.30 ± 1.30	2.98 ± 1.53
	anterior	3.28 ± 2.36	2.89 ± 1.67	3.85 ± 2.31
superior	mid x	3.04 ± 1.82	2.16 ± 0.98	2.56 ± 1.70
	posterior	3.10 ± 1.35	2.34 ± 1.18	3.04 ± 1.02

presented from inferior to superior. Each transverse slice has 9 distance values.

For the pre-plan to intra-operative displacement, the seeds near the medial line of the prostate (the z axis) moved slightly more on average. Note that no directional information can be drawn from this. For intra-operative to post-implant displacements, there were no significant differences in the amount of motion between the different subregions. In agreement with the average patient data, the intra-operative misplacement was greater than the post-implant movement in all regions.

Table 4.4: Pre-plan to intra-operative misplacement direction results. Values with a mean value to standard deviation ratio greater than 0.95 are in **boldface**

Average misplacement direction vectors (x,y,z) (mm)				
		left	mid y	right
inf	ant	(0.33,0.54,**-3.87**)	(-0.01,-1.47,**-4.14**)	(-0.51,-1.59,-2.88)
		±(2.36,2.85,**1.79**)	±(2.59,2.55,**4.20**)	±(2.05,2.06,3.15)
	mid x	(-0.24,0.02,0.31)	(0.94,0.31,2.03)	(-0.70,-0.73,0.31)
		±(1.55,2.01,3.92)	±(1.48,2.16,5.56)	±(1.96,2.14,3.56)
	post	(0.41,1.01,1.87)	(0.21,-0.05,**3.47**)	(1.40,0.07,0.55)
		±(2.43,1.85,2.67)	±(3.33,1.14,**2.55**)	±(2.61,1.78,3.22)
mid z	ant	(**1.63**,0.15,**-3.83**)	(1.90,-0.69,-3.71)	(0.42,-0.04,**-4.06**)
		±(**1.53**,2.47,**1.85**)	±(2.31,2.73,4.82)	±(2.48,1.82,**3.46**)
	mid x	(0.10,-0.97,0.70)	(-0.13,-0.28,3.21)	(-0.79,0.96,0.57)
		±(2.09,1.87,4.15)	±(1.86,2.36,5.75)	±(2.52,2.49,3.92)
	post	(0.29,-0.07,1.45)	(-0.60,0.54,**3.46**)	(0.00,1.15,0.96)
		±(2.12,2.12,2.57)	±(2.83,1.41,**2.74**)	±(1.84,2.08,4.01)
sup	ant	(**3.07**,-1.48,**-3.51**)	(**2.58**,-0.60,-3.56)	(1.68,2.34,**-2.74**)
		±(**2.02**,2.47,**1.51**)	±(**2.31**,3.16,4.28)	±(2.64,2.63,**2.86**)
	mid x	(0.12,-1.79,0.36)	(0.11,0.62,2.58)	(-0.70,2.07,0.51)
		±(2.60,2.12,4.02)	±(2.36,2.35,4.72)	±(2.77,2.80,3.53)
	post	(-0.41,-0.40,1.35)	(-2.07,0.44,**3.76**)	(-1.26,1.76,0.87)
		±(1.99,2.45,2.88)	±(2.25,1.59,**2.69**)	±(1.99,2.97,4.01)

Displacement Vector Results

It was noted that different magnitudes of displacement occurred in different regions of the prostate. The average displacement vectors for each of the 27 subregions was computed. Tables 4.4 and 4.5 summarize the general displacement directions seen. The displacement vectors are visually illustrated in Figures 4.7 and 4.8. The standard deviation ellipsoids are drawn in separate plots where each ellipsoid is centered in its respective region. Note that for the post-implant movement vectors, the axis labels indicate the position of the sub-regions but the vectors themselves have been scaled by 2 so that they can be seen. The intra-operative misplacement vectors are to scale.

As with the scalar measurements, the directional displacements from intra-

Table 4.5: Intra-operative to post-implant movement direction results. Values with a mean value to standard deviation ratio greater than 0.95 are in **boldface**.

Average movement direction vectors (x,y,z) (mm)				
		left	mid y	right
inf	ant	(0.71,0.57,-0.38) $\pm$(1.99,1.16,2.37)	(1.20,-0.00,-0.09) $\pm$(1.56,0.85,3.83)	(0.29,-0.27,-0.41) $\pm$(1.91,0.77,3.03)
	mid x	(0.38,0.48,0.18) $\pm$(2.39,1.13,2.19)	(1.75,-0.05,0.12) $\pm$(2.18,0.98,1.35)	(0.39,-0.40,0.93) $\pm$(2.00,1.29,2.81)
	post	(-0.01,**1.09**,0.36) $\pm$(1.40,**1.15**,2.31)	(0.66,0.04,0.86) $\pm$(2.05,0.68,1.89)	(0.08,**-1.67**,1.04) $\pm$(1.73,**1.44**,2.30)
mid z	ant	(-0.38,-0.12,-1.13) $\pm$(1.31,1.06,2.91)	(0.70,-0.06,-1.29) $\pm$(1.26,0.74,3.59)	(0.10,0.29,-1.12) $\pm$(1.31,0.98,3.27)
	mid x	(-1.12,0.72,-0.34) $\pm$(1.80,1.53,2.42)	(-0.02,0.15,-0.66) $\pm$(0.46,0.74,1.57)	(-0.72,-0.33,0.68) $\pm$(1.01,0.95,2.72)
	post	(-0.79,0.97,0.98) $\pm$(1.12,1.67,2.37)	(-0.59,0.03,1.36) $\pm$(0.99,0.75,1.85)	(-0.66,**-1.39**,0.97) $\pm$(1.74,**1.35**,1.82)
sup	ant	(0.53,-0.35,-1.65) $\pm$(1.25,1.24,3.22)	(**1.11**,0.08,-0.63) $\pm$(**1.11**,0.99,2.78)	(**1.34**,0.59,-0.50) $\pm$(**1.33**,1.31,3.85)
	mid x	(-0.69,0.11,-0.98) $\pm$(2.07,1.26,2.32)	(-0.72,0.07,-1.03) $\pm$(1.41,0.94,1.26)	(-0.11,-0.15,0.10) $\pm$(1.63,1.14,2.36)
	post	(-0.08,0.49,0.14) $\pm$(2.01,1.40,2.32)	(-0.34,-0.05,0.23) $\pm$(1.42,0.93,1.99)	(-0.48,-1.00,0.41) $\pm$(1.97,1.46,1.75)

operative to post-implant were smaller than in the pre-plan to intra-operative case. The significant intra-operative misplacement results can be summarized as follows: *(i)* inferior displacement of lateral anterior seeds, *(ii)* superior displacement of medial posterior seeds and *(iii)* anterior misplacement of superior anterior seeds. For the post-implant movement there is: *(i)* inward lateral movement of inferior posterior seeds and *(ii)* anterior movement of superior anterior seeds.

4.3.3 Preliminary Fluoro to Ultrasound Registration Results

Needle matching is required as a preliminary step towards registering the fluoro seed reconstructions to ultrasound volumes. This needle matching is shown for patients 9 and 13 in Figure 4.9. The needle matching was used to match the avail-
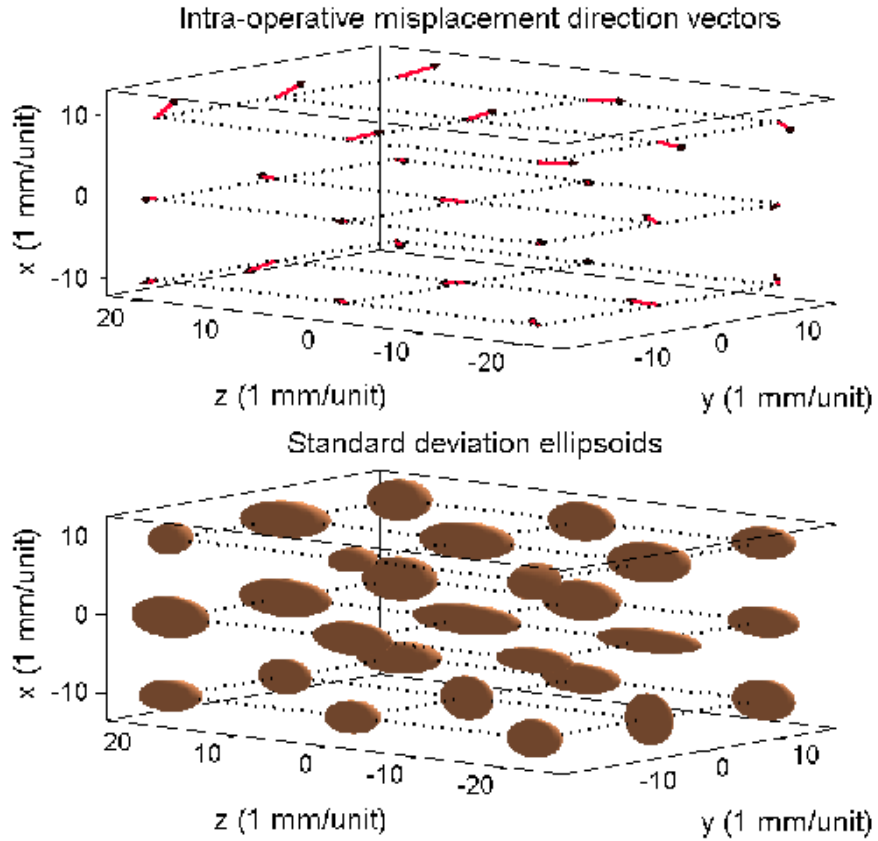
Figure 4.7: Intra-operative misplacement vectors (above) and the standard deviation ellipsoids (below).

able seeds found in ultrasound with the corresponding seeds found in fluoro. The unmatched seeds were then removed so that rigid point set registration could be performed on the remaining seeds.

Moradi *et al.* completed the registration process by accounting for prostate warping with the TRUS probe fully inserted and then using both the ICP method as well as the GMM method to perform the registration. An average post-registration distance of ∼3 mm was found in both cases. The results did not change significantly using the "leave-one-needle out" validation method [48]. This verifies that
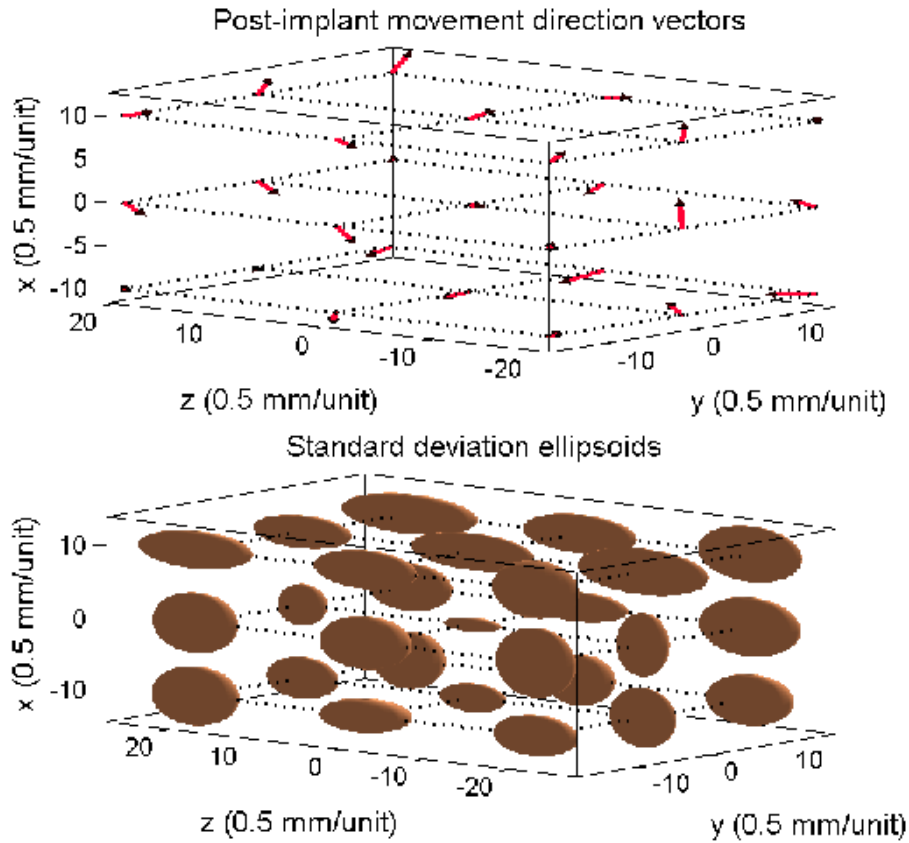
Figure 4.8: Post-implant movement vectors (above) and the standard deviation ellipsoids (below). The units in brackets correspond to the vector lengths and not the subregion positions. They are used to remind the reader that these vector lengths are doubled to make them visible.

the needle matching method used to for initial seed matching that is needed to perform full registration works.

4.4   Conclusions and Displacement Trend Hypotheses

A chain of techniques have been presented that allow seed displacement calculation as well as registration of fluoro to ultrasound. The needle track detection algorithm
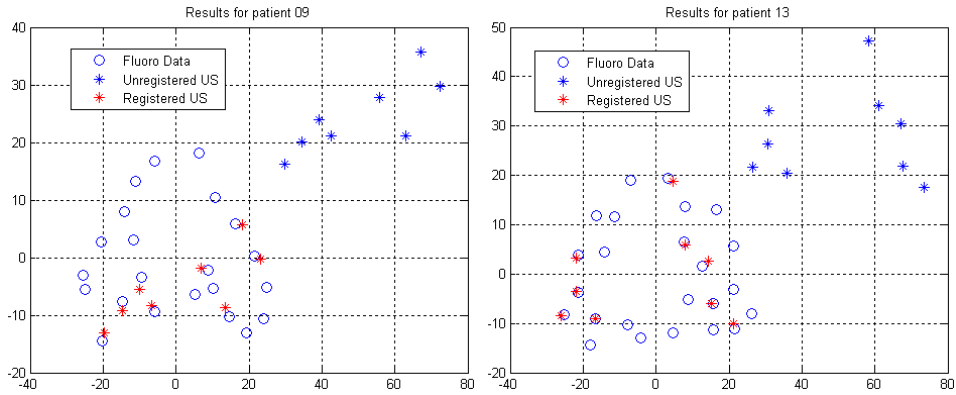
Figure 4.9: Needle matching used to align the fluoro and ultrasound data match the detected seeds

described in Chapter 3 plays a crucial role in achieving both these objectives.

The "leave-one-needle-out" method performed by Moradi *et al.* validates the needle matching method that is used to register fluoro data to ultrasound. With this registration the true potential of intra-operative planning can be realized.

The seed displacement computation, like the needle track detection algorithm, has been shown to meet all of the intra-operative planning requirements (fast, automatic and reliable). It is therefore a perfectly viable method to detect intra-operative misplacements especially with registration of fluoro to ultrasound.

Part of the first objective of this thesis was to determine if trends existed that could be compensated for before a needle is inserted. The next set of conclusions are hypotheses for potential trends seen in the displacement data.

For the pre-plan to intra-operative comparison, several regional displacements were noted. The larger amount of misplacement for seeds near the medial line is most likely due to the fact that this is the longest part of the prostate giving the oncologist more leeway to steer the needles. There is no directional trend to this placement which suggests that it is not due to needle or prostate movement. Similarly, the inferior misplacement of anterior seeds and superior misplacement of posterior seeds is also likely due to oncologist tendencies. There is a lack of implantable tissue in the anterior superior quadrant (close to the bladder) and so

seeds are deliberately placed more inferiorly. The greater retraction of lateral anterior seeds is due to the presence of the pubic arch which forces a shallower implant. The divergence of the rectum from the prostate in the superior posterior quadrant leads to a tendency to "over-plan" the medial superior region on the posterior side.

The anterior misplacement of superior anterior seeds can be explained either by prostate rotation or needle deflection. Any transverse displacement of the seeds could be due to needle deflection. It is expected that this effect would be most visible with superior seeds. However, this does not explain the anterior direction of the misplacement. Therefore, assuming that it is due to prostate movement, the base would have to rotate posteriorly during insertion to observe this displacement. This would suggest that the prostate is held more rigidly by the TRUS probe - which is on the posterior side, allowing downward rotation of the gland and so upward motion once the needle is removed - than the pubic arch.

For the intra-operative to post-implant comparison the first directional conclusion can be drawn from the lack of a global outward seed displacement. This suggests that inflammation has little or no effect for immediate post-implant seed movement. The only outward motion is seen with anterior movement of superior anterior seeds. This could be due to pressure from the bladder on the superior side of the gland when the patient pose changes from dorsal lithotomy to supine. Inward lateral movement of inferior posterior seeds must also be due to change in patient pose although further analysis of the forces on the gland during the change is needed to verify this.

In general the results show that intra-operative seed misplacement is larger than post-implant movement. This confirms results from Chng *et al.*[15], who explain the large impact that both prostate rotation and needle deflection have. This also agrees with work done by Wan *et al.* to evaluate needle deflection [79] and by Lagerburg *et al.* who evaluate prostate rotation during the insertion of needles [40]. Su *et al.* performed a study on the effect of seed misplacement on the delivered dose using random noise to model the misplacement instead of actual measurements [69] and found minimal changes in the D90 measure with misplacements of up to 4mm. However, the random noise model does not include the trends presented here. The seed displacement trends found here could therefore but incorporated into a similar study to verify these results.

Regional, directional displacement measurement techniques have been presented for seeds in prostate brachytherapy. The hypotheses described here need further confirmation from more specialists and more data may be needed to determine real trends. However, the seed displacement measurement methods provide all the tools needed to automatically compute displacements in a larger patient study to further understand variations in dose distributions from the pre-plan. The techniques described can be used to collect and measure trend data as well as to accurately detect misplacements intra-operatively. Measuring seed displacements is needed for intra-operative planning so that an oncologist can compensate, either before insertion to allow for known displacement trends or immediately after insertion if misplacement is detected. However, this is only possible if change in dose coverage due to these displacements are known relative to the target volume itself. The verified fluoro to TRUS registration method presented in this chapter is shown to be a suitable solution to this issue. It should be noted that the same registration technique can be used to register CT to TRUS (including the warp compensation [7, 48]) which would be needed to make sense of post-implant movement and migration. The significance of being able to do this registration is that the target volume is visible in the ultrasound images while not in fluoro or CT. However, the relatively low image quality, characteristic of regular B-mode ultrasound images can make it difficult to delineate the prostate and especially difficult to view tumours. In fact, the registration would not be very useful if the prostate could not be segmented in the ultrasound images. It would be convenient therefore to provide a potential intra-operative planner with a more intuitive display of the ultrasound images with automatic delineation of the target areas. Chapter 5 describes an approach to complete the intra-operative planning process using ultrasound elastography to enhance the target volume visualization.

Intra–operative misplacement

Post–implant movement
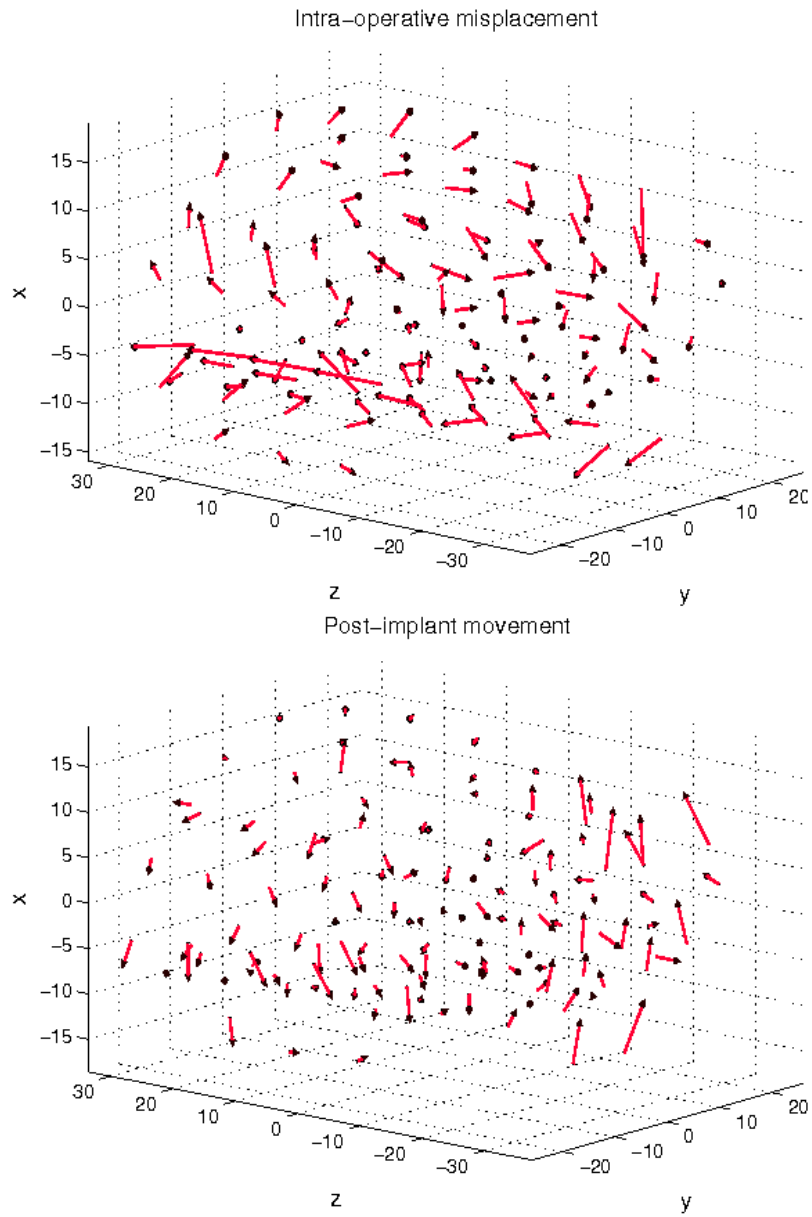
Figure 4.10: Pre-plan to intra-operative seed misplacement results for patient 4.

55

Chapter 5

Ultrasound Elastography for Prostate and Tumour Delineation

5.1 Introduction

Delineation of the target volume in ultrasound is required for intra-operative planning and is addressed in this chapter. Prostate segmentation in ultrasound is currently required during the pre-plan stage of most prostate brachytherapy procedures. Contouring is needed to determine how and where to place seeds so that the prostate will be sufficiently irradiated. For intra-operative planning to work this process must be brought into the operating room. In fact, even with accurate misplacement detection and registration of fluoro to TRUS (see Chapter 4), if prostate segmentation in the ultrasound images is not possible then the whole planning process cannot work.

Providing a method to delineate the target region intra-operatively also solves another issue that leads to errors in seed positioning. Chapter 4 presents a method of computing errors that arise from needle or prostate movement, prostate inflammation or change in patient pose. However, the first of the issues summarized in Chapter 1 has not been addressed yet. This is the fact that the shape and position of the prostate may have changed in the time between the pre-plan scan and the operation itself. Intra-operative prostate segmentation and cancer detection would allow for an "Intra-operative pre-plan" [52] which would remove this concern and
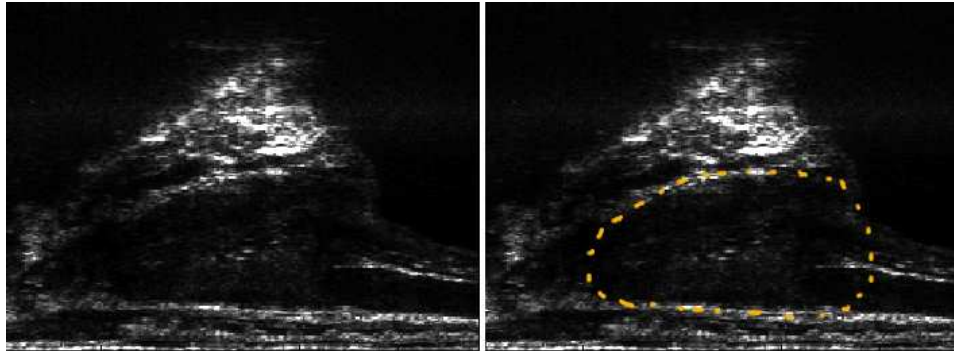
Figure 5.1: A sagittal B-mode ultrasound image of the prostate with (right) and without (left) manual contouring.

has been shown to produce better results that regular pre-plans [47].

Figure 5.1 illustrates how it is not trivial to segment the prostate in a traditional B-mode image due to low resolution and blurred boundaries. Accurate segmentation in ultrasound has therefore been studied widely [1, 7, 29, 42, 45]. Incorporating this into an intra-operative planning environment requires that it also be performed rapidly with as little manual interaction with the software as possible.

Active Shape Modeling (ASM) [29], deformable shape modeling [26], region growing [45] and warped ellipse fitting [7, 42] are all automatic segmentation algorithms that could work for the purpose of intra-operative planning. However, all these methods require some sort of manual initialization. This could still work since the user input is minimal but more research would have to be done on how feasible it is.

In this chapter, another technique that removes the initialization problem is presented. Quantitative or absolute ultrasound elastography is used to measure and display the stiffness of the different regions which inherently delineates the target region since the prostate tissue has different elastic properties from its surrounding region. Another incentive to use elastography is that computing the stiffness of the tissue also allows for potential visualization of tumourous regions within prostate as well as the gland itself. Knowledge of the location of the cancerous regions can help plan a more case-specific seed distribution. It could even allow localized

treatment by boosting dose levels in tumourous regions or sparing more healthy tissue as is proposed in the field of focal therapy [2, 18, 50].

Krousoup *et al.* suggest that there is a direct relationship between tissue stiffness and the cell density in tissue [39]. Since cancerous tissue has a higher cell density (more cells per unit volume) than non-cancerous tissue, it follows that measurement of the rigidity of the tissue should help with cancer detection. Indeed, the use of elastography in targeted prostate biopsies has already been investigated [53]. Methods to compute the relative elasticity (stiffness is measured in comparison to surrounding tissue) in real time have been studied previously [38, 54, 56, 63]. However, it would be more useful to compute the absolute elasticity (measuring the Young's modulus) of the different regions so that results don't vary too much between cases. This also allows for better comparison between different datasets for further investigation. The implementation of an algorithm used to compute the Young's modulus using ultrasound imaging will be presented in the following sections. Mahdavi *et al.* have presented a fully automatic approach for prostate segmentation which uses elasticity measurement to initialize the segmentation [43].

A real-time stiffness display, or elastogram, provides a more intuitive view of the prostate region. Overlaying registered intra-operative or pre-plan seeds would then give an oncologist immediate feedback on the quality of a given implant without having to explicitly segment the target region. Alternatively, the elastograms could be used to initialize any of the automatic segmentation algorithms described so that the dose coverage can be measured.

5.2   Computing Absolute Elastography in Ultrasound

The basis of the elastography algorithm is that materials with different stiffnesses respond differently to external stress, whether it be static compression or dynamic excitation. The idea is to measure this response and then convert it into a measurement of the rigidity of the material.

Dynamic excitation at a given temporal frequency generates displacements within a given material. It can be shown that resulting displacements can be represented as the sum of the gradient of a scalar potential, ϕ, and the curl of a vector potential, ψ [9, 36]. ϕ corresponds to a "dilatational" wave and ψ corresponds to

a "shear" wave. The spatial frequencies, or wavenumbers, of the dilatational wave, k_d, and the shear wave, k_s, are functions of the Lamé parameters of the material which describe its viscoelastic properties. k_d can usually be computed directly and so the viscoelastic properties (including the Young's modulus) of specific points in a volume can be found by computing the local three-dimensional spatial frequency, k_s, from the measured displacement data. The local frequencies can be computed using lognormal quadrature filters as Local Frequency Estimators (LFE) [10, 35]. Another method for performing the inversion required to compute the local frequency is to use a Travelling Wave Expansion (TWE) model of the solution to the wave equation (a sum of waves travelling in every direction with the same spatial frequency) [9]. Measured displacements can be fitted to the TWE model to solve for the spatial frequency and so the Young's modulus.

The algorithm is implemented as follows: A specific excitation frequency, f_e, can be used to generate motion in the tissue. A tissue motion tracking algorithm [8, 19] is then used to create a series of displacements per pixel as a function of time from N_{fpp} frames per plane. Assuming linearity, all the motion has the same temporal frequency (f_e). Therefore, a complex exponential describing just the phase and amplitude of the motion at each pixel can be used to represent the response of the system. This complex exponential is called a "phasor". In this way, a single phasor displacement image is generated from the set of N_{fpp} time series displacement images which can reveal any travelling waves that are created in the tissue. The waves seen in a phasor displacement image, however, are only 2D projections of the actual travelling waves created by the excitation. Therefore, 2D phasor images are computed for a series of N_{ppe} planes creating a 3D volume sweep. The set of N_{ppe} 2D planes are interpolated into a Cartesian grid so that the 3D waves can be seen. The local spatial frequencies of these waves at every point in a given plane are computed using LFE applied to the 3D Cartesian block. This creates a single elastogram (the "ppe"subscript stands for "planes per elastogram"). This process is repeated for an entire volume producing N_E elastograms from N_p planes. Note that $N_E = N_p - N_{ppe} + 1$.

Note that this means that a few planes must be acquired before the first elastogram is computed since a block of 2D phasor images is needed. However, a relative elasticity or strain image can still be generated directly from each 2D pha-

sor image. Therefore the number of strain images $N_{RE}=N_p$.

The described inversion algorithm has been previously implemented for free hand ultrasound [10]. This study includes the use of a Graphical Processing Unit (GPU) which takes advantage of parallel processing to speed up the process ao that it can be used in real-time. The next section describes how it has been implemented for elasticity measurement of the prostate region.

5.3 System Implementation for Prostate Elastography

This section describes the system design used to implement Baghani *et al.*'s algorithm to compute absolute elastography [10] for the prostate. The entire system is summarized in figures 5.6 and 5.7 but is described in the following sections first.

5.4 The BK Ultrasound Machine

A BK ultrasound machine (BK Medical, Herlev, Denmark) is used with the 8848 4-12 MHz TRUS linear transducer in this study. It provides extremely high image resolution which allows better tissue tracking which should increase the reliability of the system. It is also already used at the Vancouver Cancer Care (VCC) at the BCCA which makes it possible to use the same ultrasound machine that is used in standard clinical routine and therefore can shorten significantly the data acquisition during the procedure.

Raw Inphase Quadrature (IQ) data can be read from the machine but external control of the acquisition is not possible. Therefore the default imaging parameters are kept with the highest sampling rate (The depth of acquisition is 5.6 cm and the sampling rate 42.66 Hz) and the IQ data is continuously read into an external PC through a DALSA Xcelera-CL PX4 Full frame grabber card (Teledyne DALSA, Waterloo, ON). Figure 5.2 shows an image of the BK ultrasound machine with the TRUS probe and the raw data output port.

The main issue with not having an external control of the image acquisition is with the tissue tracking algorithm. Excitation frequencies are usually around $\sim$100 Hz which are *higher* than the sampling rate. The Nyquist criterion states that the sampling rate must be at least twice the frequency of the signal to prevent aliasing. Therefore, there needs to be a method of increasing the sampling
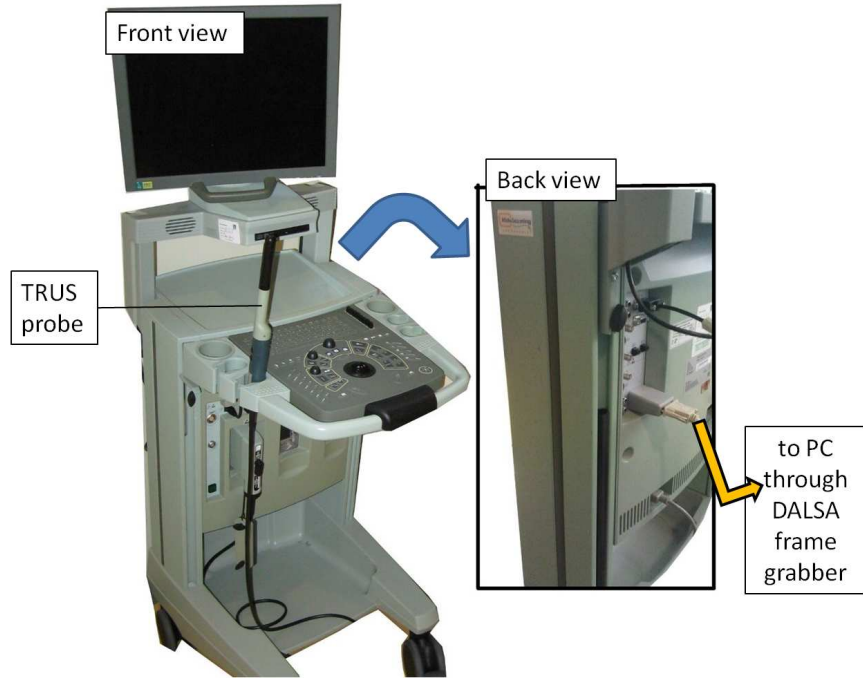
Figure 5.2: The BK ultrasound machine. The raw data output port located at the back of the machine is shown in the inset image.

frequency. One example of this is to use sector-based acquisition similar to the acquisition used for Doppler imaging [8]. However this requires control of the transducer crystals which is not possible with the constraints of the BK Medical UI. A band pass sampling algorithm described by Eskandari *et al.* is therefore used which allows phase and amplitude reconstruction with sampling frequencies that are lower than the excitation frequencies. The following equation from [19] more accurately describes the limitations for the sampling frequency, f_s:

$$\frac{2f_e + B}{m + 1} \leq f_s \leq \frac{2f_e - B}{m} \tag{5.1}$$

where f_e is the excitation frequency, B is the allowed bandwidth of the excitation frequency, and m is any positive integer. This means that for a given sampling frequency, the allowable excitation frequencies are restricted to a set bands (com-

61

Table 5.1: Excitation frequencies that allow tissue tracking with band pass sampling for a frame rate of 42.66 Hz.

Excitation Frequency (Hz)		
Minimum	Maximum	Center
69.0	80.3	74.7
90.3	101.7	96.0
111.7	123.0	117.3
133.0	144.3	138.6
154.3	165.6	160.0
175.6	187.0	181.3
197.0	208.3	202.6
218.3	229.6	224.0

puted for different values of *m*). Still, as long as the excitation frequencies do fall within these bands, the algorithm allows for accurate tissue tracking within the allowed bands. Table 5.1 summarizes the allowed bands for the BK sampling rate (42.66 Hz).

Another consideration that needs to be taken into account is the relationship between the data collected for different planes in a volume. From section 5.2, phasor displacement images are computed for each plane. In order to study these displacements in 3D, the phasor planes must be in phase with each other. In other words, the excitation cycle must be the same for each plane. If the acquisition could be turned on and off then this could be achieved by only beginning to read data for a plane when the excitation is at the start of a cycle. Since there is no control of when the data is to be outputted, post-acquisition phase compensation is used. The compensated phasor image, PC_i, for plane i is computed as:

$$PC_i = P_i e^{(-2\pi f_e i(t_i - t_0))} \tag{5.2}$$

where P_i is the uncompensated phasor image, t_i is the time stamp for the first frame of plane i and t_0 is the time stamp of the first frame of the very first plane [8].

To summarize the collection process for absolute elastography with the BK ultrasound machine: N_{fpp}=20 frames are collected per phasor image. N_{ppe}=22
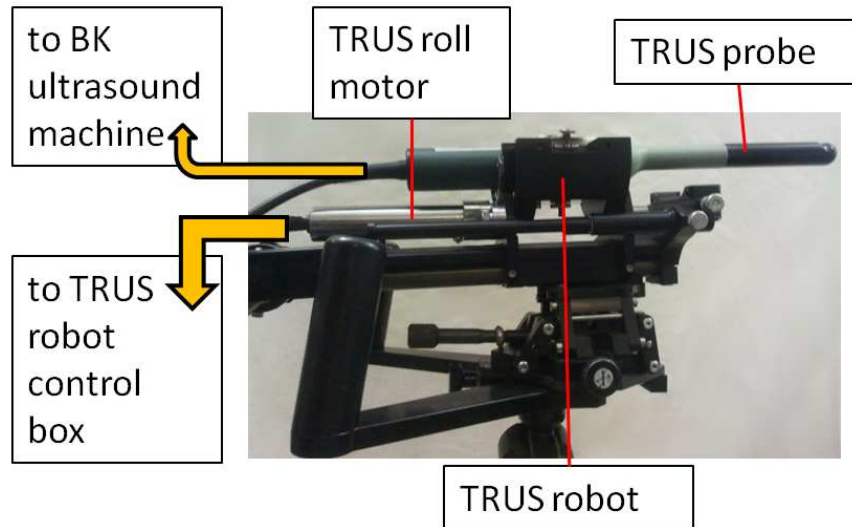
Figure 5.3: The TRUS robot with the BK transducer.

phasor planes are used to compute one elastogram. A total of N_p=100 planes are collected producing N_E=79 elastograms for the entire volume. If strain imaging is used instead of absolute elastography N_{SE}=N_p=100.

5.5 The TRUS Roll Mechanism

A previously designed TRUS roll robot is used in this study. A cradle specifically designed to hold a TRUS probe is attached to a regular TRUS mount. A "roll" motor is used to sweep the cradle and is equipped with an optical encoder so that the position can be accurately controlled by a "TRUS robot control box". A motor control Figure 5.3 shows a side view of the TRUS robot with the BK transducer held in the cradle.

A volume sweep is created by rolling the TRUS probe in 0.9^o increments N_p=100 times. The full sweep angle is therefore $0.9*N_p$=90° from - 45 ^{o} (patient right) to + 45 ^{o} (patient left). The probe remains at a given roll location until N_{fpp}=20 frames have been acquired.

5.6 The Excitation Mechanisms

A different excitation mechanism is needed for the elastography system depending on the type of elasticity that is desired.

Strain, or relative elasticity is measured from 2D planes and therefore requires excitation that is parallel to the imaging direction (any wave propagation that is not cannot be measured). This requires transrectal excitation which works well because there is close contact with the prostate itself and also takes advantage of the high image resolution in the axial direction. This method is not suitable for absolute elastography since the excitation direction changes as the TRUS roll robot sweeps. The inversion algorithm requires a static excitation source for which it can provide a solution for the frequency and direction. Therefore a transperineal exciter is used.

5.6.1 Transrectal Strain Vibration

A DC motor with a an offset mass on its shaft is mounted onto the cradle of the TRUS robot transducer cradle. The offset mass pushes the cradle down against a spring and then releases it as the strain vibration motor rotates forcing it to oscillate vertically. This causes the probe itself to oscillate, exciting the tissue perpendicular to imaging direction. The excitation frequency used for strain imaging is usually much lower than the excitation for absolute elastography system and is set to ∼10 Hz for this system.

5.6.2 Transperineal Shaker

For absolute elastography, a voice coil shaker is used to excite the perineum of the patient (or the model of the perineum in a phantom). A CIVCO flexible arm (CIVCO Medical Solutions, Kalona, IA) is used to mount the shaker to the patient table. The flexible arm can be maneuvered in order to provide good contact with the excitation surface and then locked into position using cable locks. Figure 5.4 displays the shaker together with the CIVCO arm. Figure 5.5 shows the transperineal exciter mechanism with the TRUS robot and BK transducer.

An Agilent U2761A function/generator (Agilent Technologies, Santa Clara, CA) is used to output the desired excitation frequencies. It will be referred to as
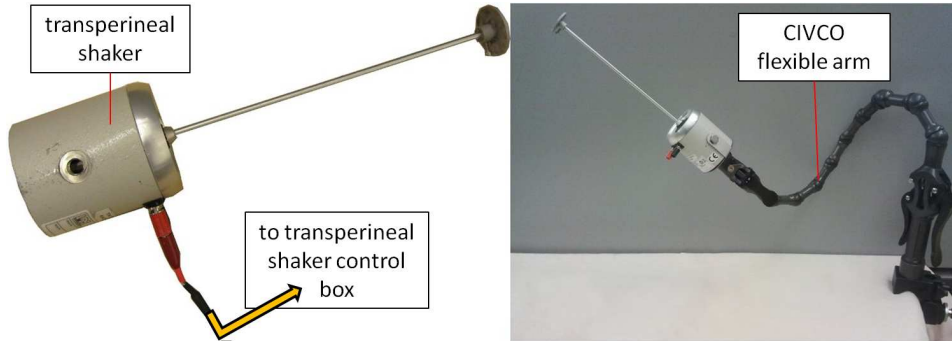
Figure 5.4: The voice coil exciter shown alone (left) and mounted to a table using the CIVO flexible arm (right).
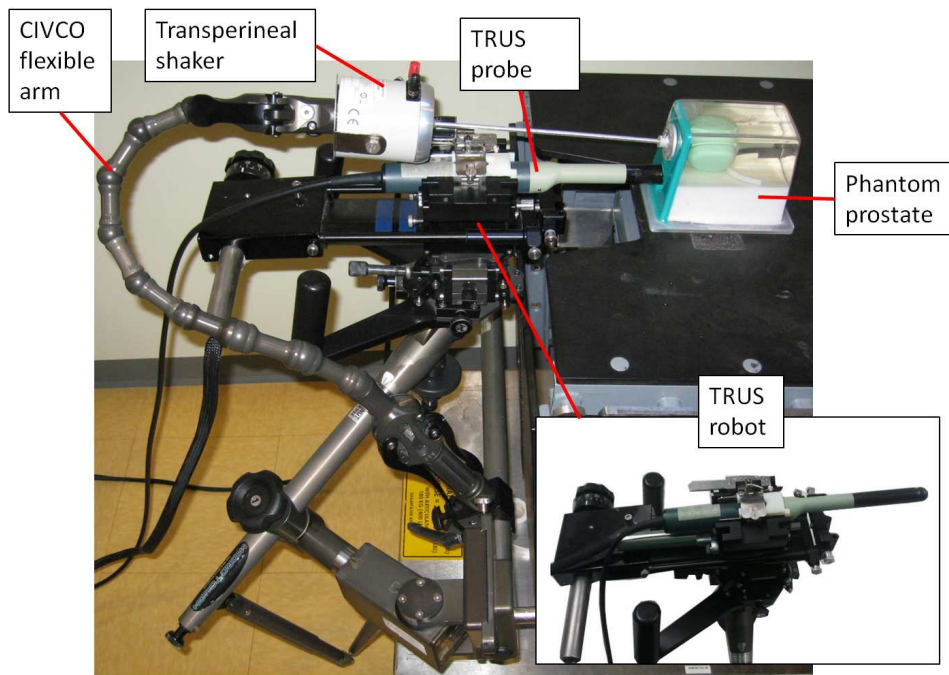
Figure 5.5: The transperineal exciter mechanism, TRUS roll robot, and BK transducer in a mock setup with a phantom.
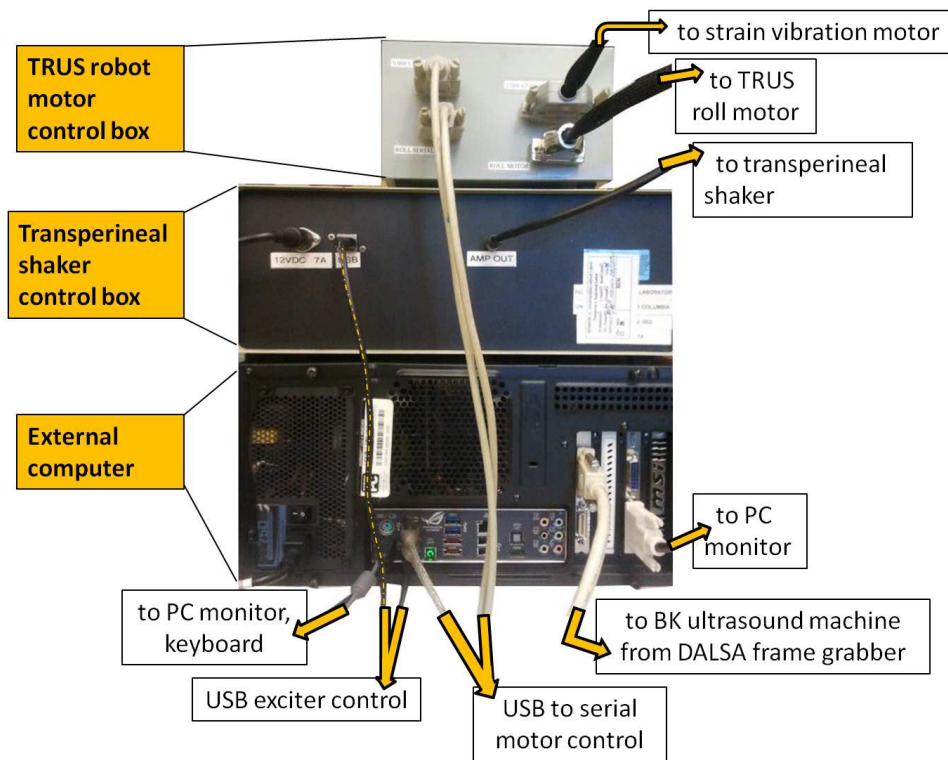
Figure 5.6: The control unit for the elastography with all the required connections.

the "transperineal shaker control box". Combinations of excitation frequencies can also be produced which allow measurement of the elastic modulus using several frequencies simultaneously. The average modulus would give a more accurate result. In this case separate phasor images are computed for each frequency at each plane.

Figure 5.6 shows how the control boxes and PC are connected. Figure 5.7 shows the complete setup during an absolute elastography sweep.

5.7 Phantom and Patient Studies

In order to check how well the elastography system is suited for intra-operative planning it was tested with both phantom and patient data. Preliminary results
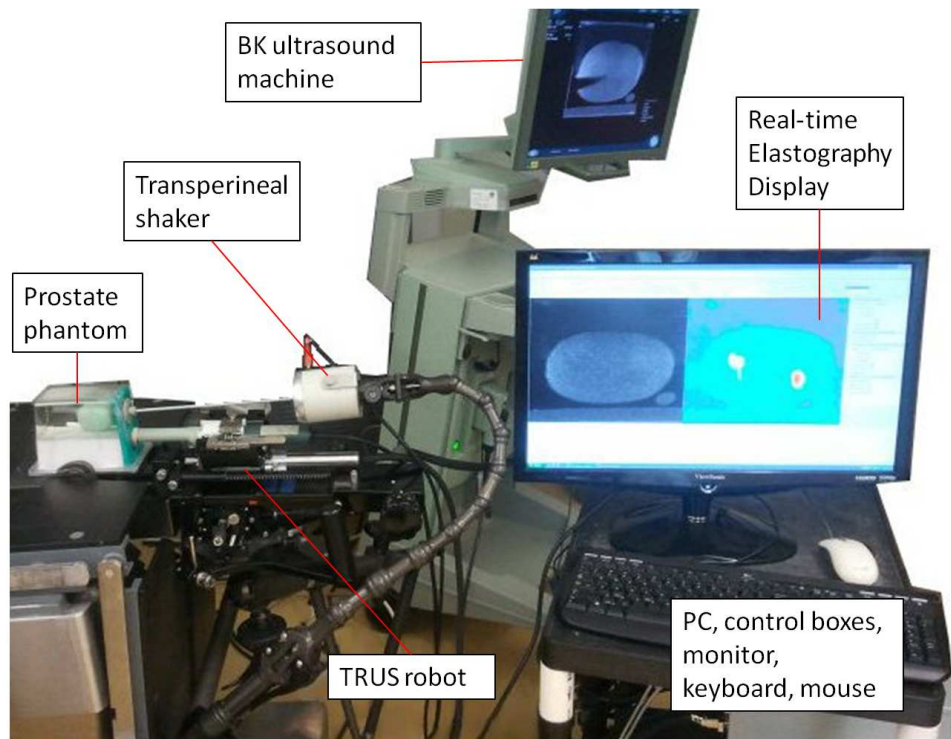
Figure 5.7: An absolute elastography sweep showing all the different electrical components. The "real-time" elastography image can be seen to be slightly different from the BK monitor image. This is due to the fact the 22 frames are required to compute one elasticity image so it lags slightly behind.

only are presented in this thesis to check if the target region is delineated well.

Both strain imaging and absolute elastography was performed on a CIRS phantom model 066 (Computerized Imaging Reference Systems, Norfolk, VA) which has 3 simulated hard inclusions. The approximate locations of the inclusions are:

1. In the "patient" right, superior, anterior region of the prostate phantom (at a sweep angle of - 5.5 ^{o}).

2. In the "patient" right, inferior, posterior region of the prostate phantom (at a sweep angle of - 4.5 ^{o}).

3. In the "patient" left, central region of the prostate phantom (at a sweep angle of $+22.5\,^o$).

Absolute elastography was performed on patients who were undergoing radical prostatectomy due to prostate cancer at Vancouver General Hospital (VGH). Institutional Research Ethics Board approval and patient consent were acquired. Results were compared to qualitative information, provided by medical residents who viewed the biopsy report, at the time of the surgery. The study was used to check both the reliability of elastography system *and* the feasibility of using it in an intra-operative environment.

Raw IQ data, time displacements data, phasor displacement data and elasticity was saved in all cases which can be used in future studies.

5.8 Results

As a demonstration of the full system, time displacements, phasor displacements, relative elasticity and absolute elasticity images are provided for the phantom. Absolute elastography results are shown for the patients. A volume sweep for absolute elastography took ∼1 minute.

In all the images shown below the horizontal axis runs from inferior to superior (i.e. the apex of the prostate is located on the left side of the image and base on the right). The vertical axis is the axial line of the ultrasound image and runs from the probe (at the bottom of the image) upward.

5.8.1 Phantom Results

The convenience of being able to test the phantom repeatedly allowed a range of frequencies to be used. Three frequencies were used simultaneously and chosen such that were each within the allowable bands from Table 5.1 and also far enough apart in baseband to be easily separated when computing phasors. The frequencies chosen were 144 Hz, 181 Hz and 208 Hz. These are all "allowed" frequencies and are measured as 16.0 Hz ($144 - 3f_s$), 10.4 Hz ($181 - 4f_s$) and 5.4 Hz ($|208 - 5f_s|$; the 180° phase shift is accounted for in the bandpass algorithm [19]) when brought to the baseband. Therefore they are far enough apart for accurate frequency reconstruction.
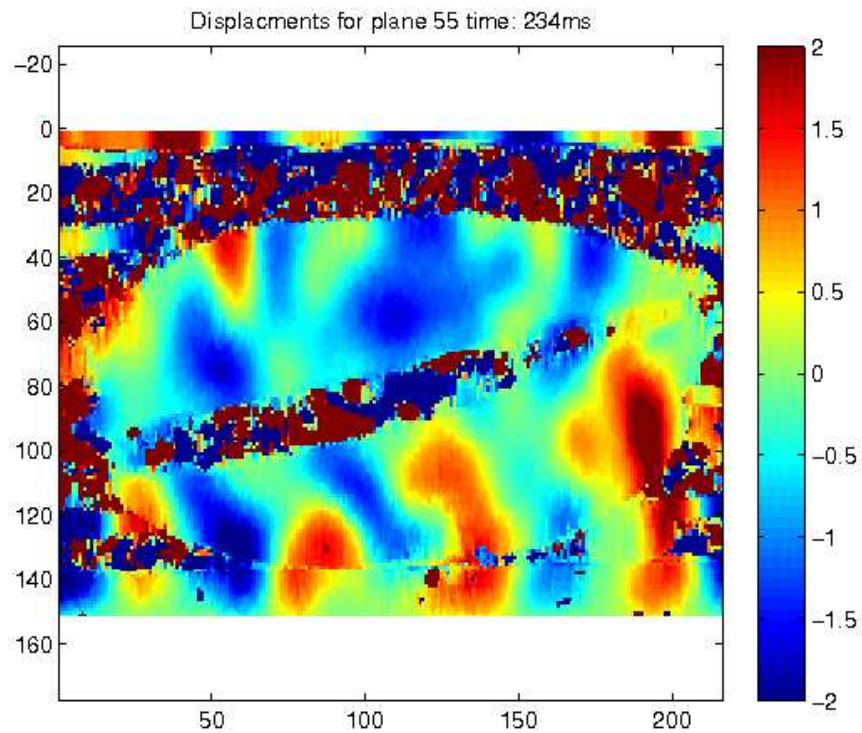
Figure 5.8: A time displacement image from plane 55 of the phantom data.

Intermediary displacement images

A single time displacement image is shown in Figure 5.8 at plane 55 (out of $100(N_p)$). This corresponds to a sweep angle of $+ 4.5\,^o$). A series of 20 (N_{fpp})of these images are used to compute a phasor displacement image at plane 55 for each frequency which is shown in 5.9.

Strain Imaging

To provide an investigation of the use of relative elasticity or strain imaging a 10 Hz excitation signal was used to excite the phantom using the strain vibration motor. Figure 5.10 shows the strain result at a sweep angle of $- 4.5\,^o$ to show both inclusions on the phantom right side.
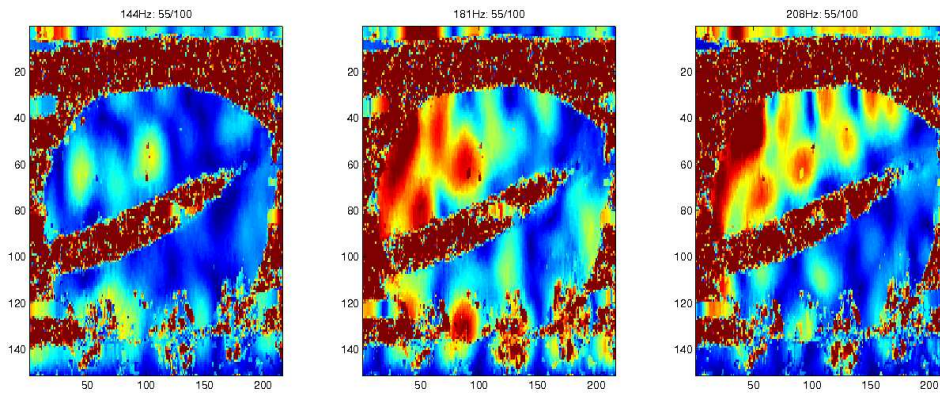
Figure 5.9: Phasor displacement of plane 55 for 144 Hz (left), 188 Hz (middle) and 208 Hz (right). The projected wavelengths can be seen to get smaller for higher frequencies.
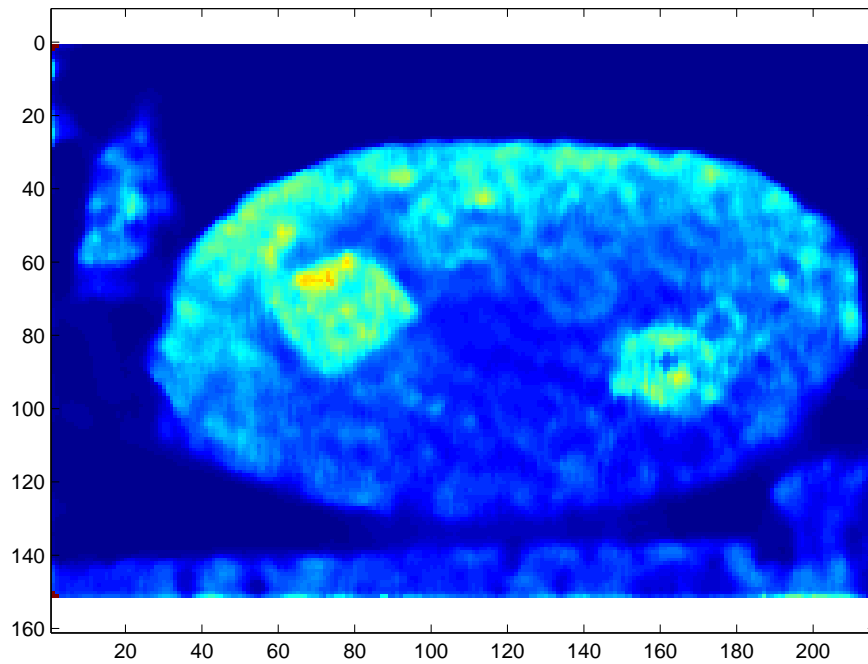
Figure 5.10: A strain image of the phantom at a sweep of - 4.5 ^{o}. Both of the inclusions located on the right side of the phantom are visible.
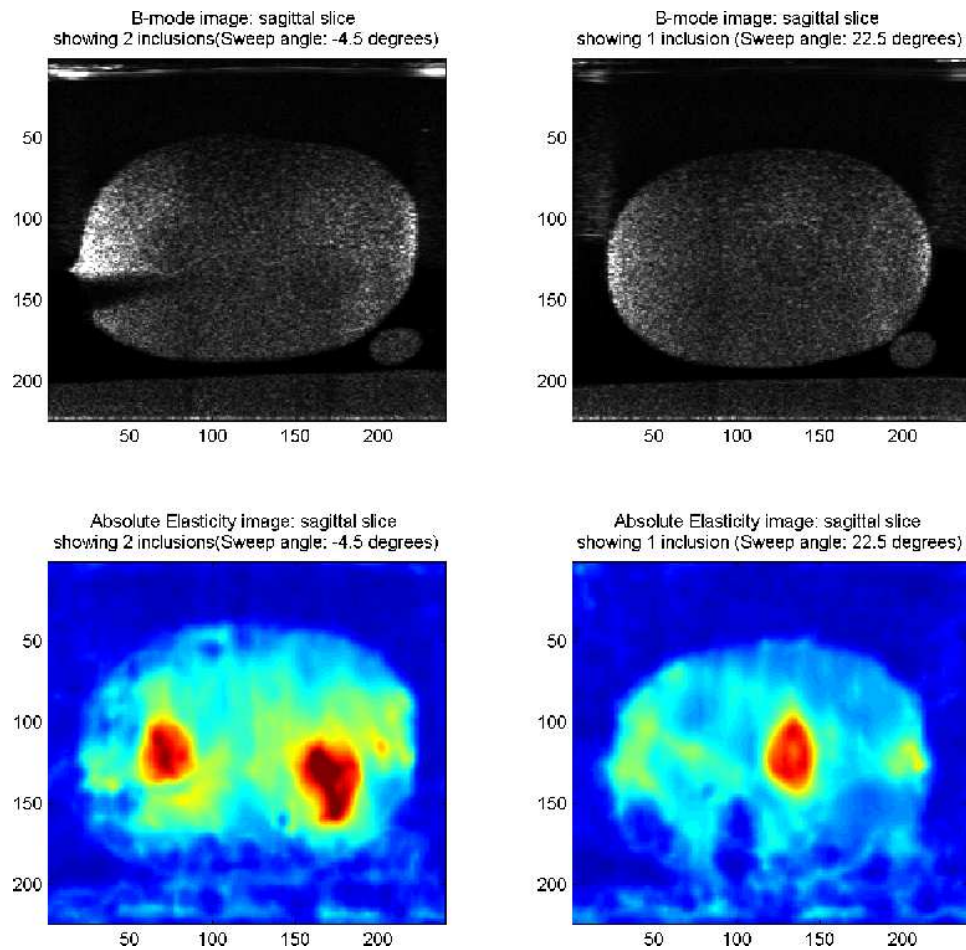
Figure 5.11: B-mode images (top) are compared to absolute elasticity images (bottom) for the phantom. The results are shown for a sweep angle of - 4.5 ^{o} (left) and + 22.5 ^{o} (right).

Absolute Elastography

Figure 5.11 shows the absolute elastography result for the angles - 4.5 ^{o} and + 22.5 ^{o} showing all three inclusions. The colourmap for the images is set from 0 kPa (blue) to 50 kPa (red). The elastic modulus was computed by averaging the results from transperineal excitation at 144 Hz, 188 Hz and 208 Hz.

71
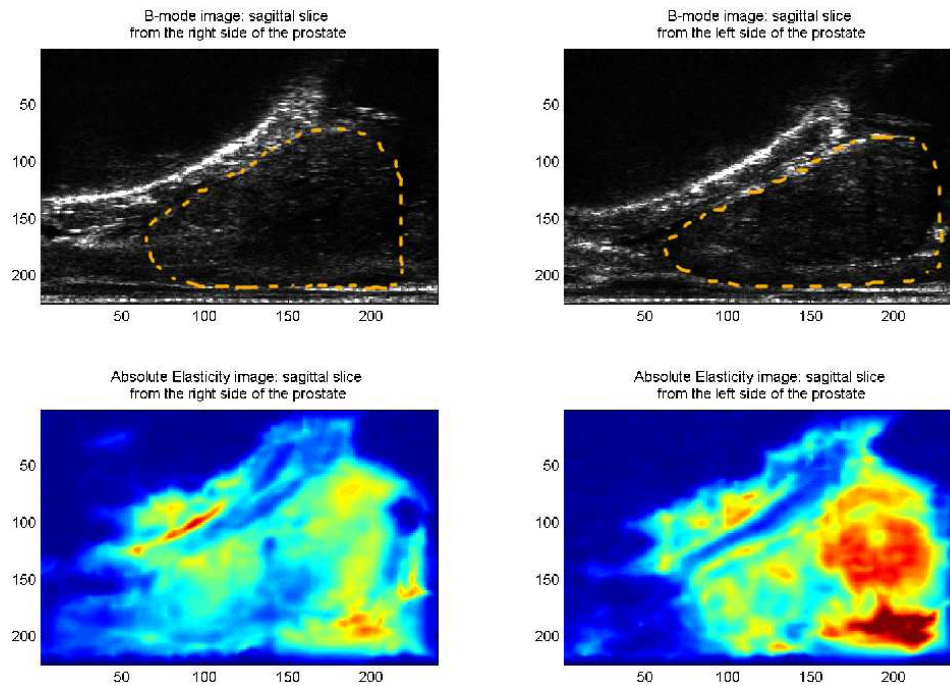
Figure 5.12: Absolute elastography results (bottom images) for patient 1 (the excitation frequency is 75 Hz). A slice from the patient right side (left images) is compared to a slice from the patient left side (right images). The B-mode images (top images) are manually contoured to show the prostate more clearly.

5.8.2 Patient Results

The absolute elastography results for 2 patients are presented in this section. Excitation frequencies of 58 Hz, 75 Hz and 96 Hz were used. However, only the 75 Hz excitation provided reliable results. The images in this section compare the elastograms to B-mode images of the same slice. Since the prostates are not clearly visible in B-mode images a manual contour is overlaid on the image to segment it.

The first patient is an older man with a large prostate. According to medical residents who viewed the biopsy report, several tumours existed on the left side of the prostate at the base. Figure 5.12 shows the result for this patient. It can be seen that the left side is much stiffer than the right side, especially at the base of the
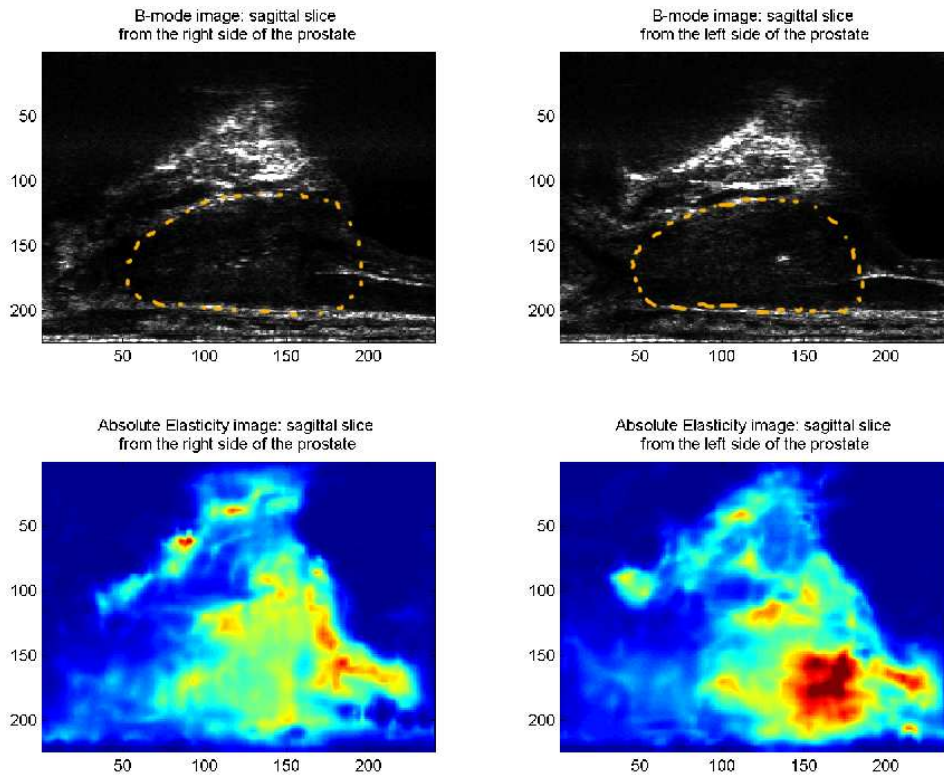
Figure 5.13: Absolute elastography results (bottom images) for patient 2 (the excitation frequency is 75 Hz). A slice from the patient right side (left images) is compared to a slice from the patient left side (right images). The B-mode images (top images) are manually contoured to show the prostate more clearly.

prostate (on the right side of the images).

The 2nd patient in this study is a younger man whose prostate is therefore much smaller (prostate volume has been shown to steadily increase with age [78]). The cancer, according to the nurses, was again located on the left side but more widely spread. Figure 5.13 displays the results for patient 2. From the absolute elasticity results, the left side of the prostate is much stiffer than the right side.

For reference, the same results for both patients are shown with uncontoured B-mode images in Figures 5.14 and 5.15, appended at the end of this chapter.

5.9 Conclusion

An elastography system has been successfully implemented and shown to work robustly. The focus of the experiments was on absolute elastography which provides quantitative results that can be used in future studies but reliable strain imaging (relative elasticity) is also provided. The strain imaging worked well for the phantom but has not been tested on patients. The system is capable of saving strain data and so more research can be done in this area.

The new absolute elastography system [9] demonstrated promising results. All the requirements for the application of intra-operative planning are met. Firstly, the time taken for a full volume sweep is ∼1 minute which is short enough for it to be used during a brachytherapy procedure.

The software also works well to enhance the target region and separate it from the surrounding region. For both the phantom and the patient data, the detected stiffer regions correlated well with the inclusions or expected tumour locations. Although much more data is required, it is proposed that an elastogram will provide a more intuitive representation of the prostate and especially of cancerous regions. When combined with seed matching and registration of fluoro to ultrasound, an oncologist would be able to view seed positions and potential misplacements with the respect recognizable stiffer regions (displayed as red) in the elastogram. This in effect allows intra-operative planning for prostate brachytherapy without the need to actually segment the prostate.

For a more calculated approach to intra-operative planning, explicit segmentation is required. Still, the visual delineation provided in the elastograms suggests that it is possible to use absolute elasticity images to initialize other automatic segmentation algorithms [1, 7, 29, 42, 45]. A fully automatic approach to prostate segmentation using this approach is described by Mahdavi *et al.* [42].

More research is still required to further validate the use of elastography. The software must be tested on prostates that have brachytherapy seeds implanted inside them to see what effect that has on the results. A transrectal excitation mechanism that remains fixed as the probe rolls would be beneficial because the excitation would take place closer to the prostate. Developing an exciter like this would add another benefit since the majority of the displacements would be in the axial di-

rection which has the best resolution in ultrasound images. One should also verify that the seeds do not cause peculiarities in the raw IQ images used to compute elasticity which could negatively impact the result. If this is the case then ultrasound elastography could not be used in between implants but could still be used in the OR just prior to the first implant.

Research on multi-frequency excitation on patient data is also needed. A wide range of frequencies could be tested for the phantom but this was not possible with the patients. It is worth finding a set a frequencies that work well so that averaging to further improve the result can be done.

The last area of future research for the use of absolute elastography for intra-operative planning for brachytherapy is to compute true correlations between the stiffness and the cancerous regions. This can be done by comparing the elastograms with pathology results from excised prostates. If a strong correlation can be made then subregions within the prostate in the elastograms can be identified as cancerous tissue. Combining this with automatic segmentation algorithms would allow for complete dose coverage of cancerous tissue in real time, using seed reconstruction from Chapter 2 [17], along with misplacement detection using displacement techniques from Chapter 4. The current system would rely on oncologist intuition to determine what the different hard and soft regions are so that registered misplacements can be compensated for. Still, the stiffness map does simplify the image to enhance the target region.
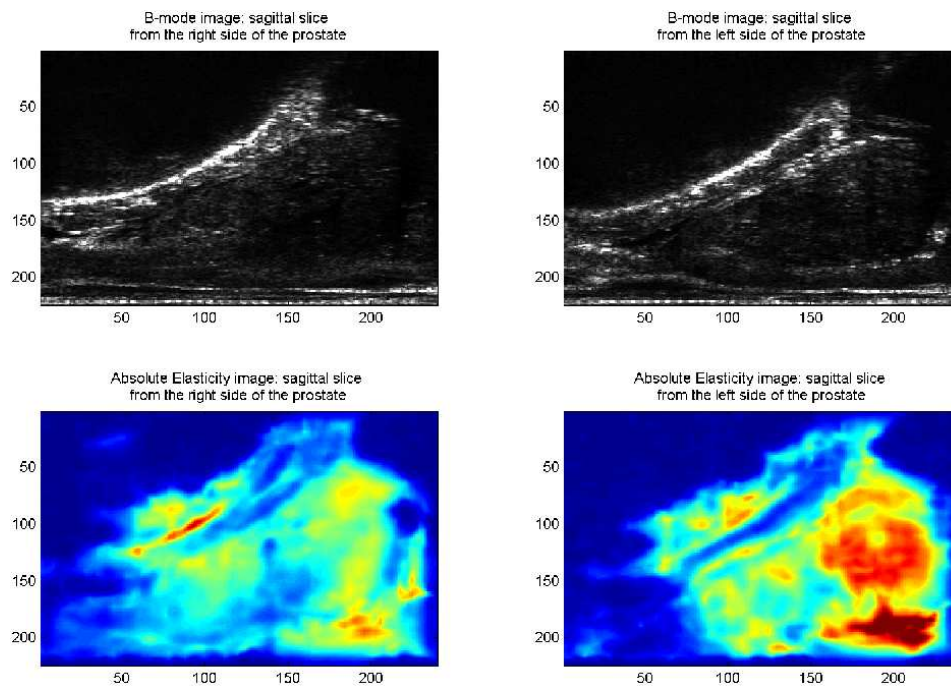
Figure 5.14: Absolute elastography results (bottom images) for patient 1 (the excitation frequency is 75 Hz). A slice from the patient right side (left images) is compared to a slice from the patient left side (right images). The elastogram enhances the target regions in the images.
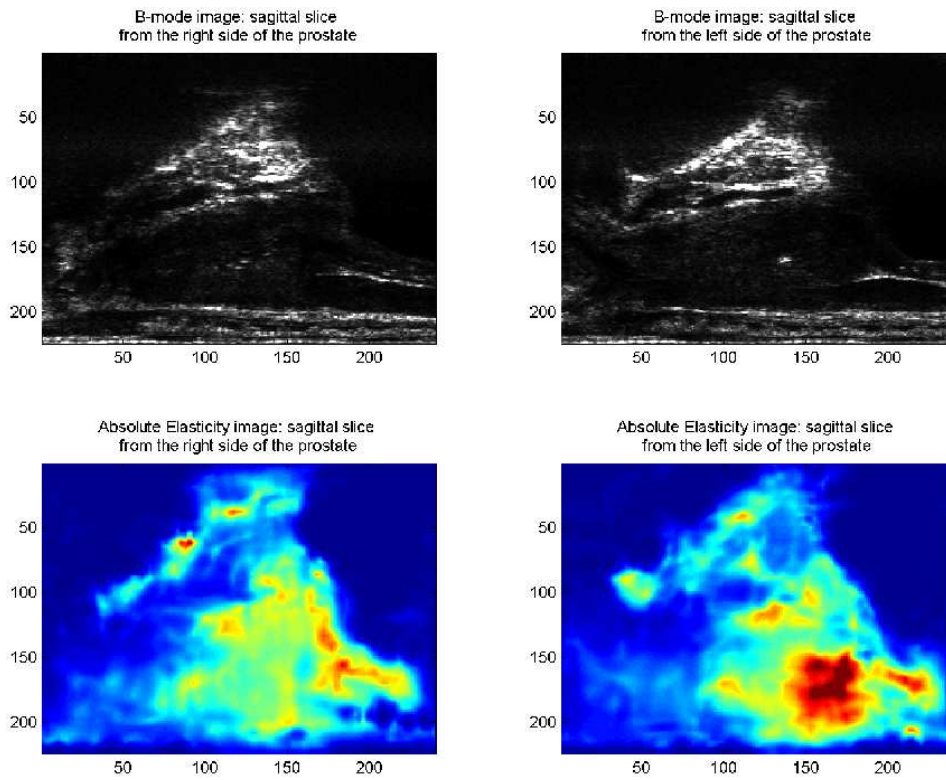
Figure 5.15: Absolute elastography results (bottom images) for patient 2 (the excitation frequency is 75 Hz). A slice from the patient right side (left images) is compared to a slice from the patient left side (right images). The elastogram enhances the target regions in the images.

Chapter 6

Conclusions

Interactive intra-operative planning is a method used to reduce misplacement errors during prostate brachytherapy [52]. The reasons why errors in seed position occur, as outline in Chapter 1 can actually be split into two types: Those that occur as a result of changes in the target volume as compared to the pre-plan and those that occur due to seed displacements during and after implantation.

In order to make intra-operative planning plausible, techniques must be used to give the oncologist fast and reliable information on the structure of the target volume as well the positions of seeds relative to the pre-plan *and* the target volume. Systems and algorithms that address these issues have been presented in this thesis. The proposed methods are purposefully chosen to make use of the imaging modalities that are already being used in standard procedures. From a clinical perspective, this is important since it is not easy to make drastic changes to the standard work flow.

A list of contributions is presented in the next subsection.

6.1   Thesis Contributions

- A real-time GUI has been developed that incorporates automatic segmentation of fluoro images used to reconstruct the intra-operative seed positions. A potential graphical display of the reconstruction is also presented. The availability of this data is crucial for intra-operative planning to work.

- A method used to simplify the representation of a 3D seed cluster by finding needle tracks has been developed. This seed matching is used to compute seed displacements which can be done in real-time and also for studies to predict trends. The major contribution of the algorithms presented is that they work reliably on intra-operative fluoro data.

- Two different registrations are presented. Firstly, implantation axis detection is used to put full seed reconstructions from fluoro, CT and pre-plan datasets into correspondence which allows seed displacement calculation. Secondly, a method to help with the registration fluoro to intra-operative TRUS which puts the seed positions and displacements into the patient coordinate system.

- A method to compute and display the absolute elasticity of a prostate volume from ultrasound has been implemented. This provides real time organ and tumour delineation which justifies the significance of the registration of fluoro to ultrasound. In addition, this provides a method of viewing the target region in the OR which means the pre-plan can be done just prior to an operation so that there are no changes in the prostate volume between the pre-plan and operating conditions. This method of pre-planning has been referred to as "intra-operative preplanning" [52].

With the above contributions a proposed intra-operative planning protocol can be developed. For example a procedure described below could be used:

1. Just prior to the the first needle implant, perform a full absolute elastography sweep to create an intra-operative preplan.

2. Adjust the intra-operative pre-plan to compensate for pre-calculated, region-dependent, displacement trends.

3. Insert a few needles (the number is subject to the oncologists discretion) into key target areas.

4. Reconstruct the seed positions using intra-operative fluoro images from 5 discrete angles. Misplacement vectors can be computed immediately as compared to the intra-operative pre-plan.

5. Perform a RP ultrasound sweep to detect seeds in ultrasound and register the ultrasound volume to the fluoro seed positions.

6. Overlay seeds or displacement vectors on elastograms (either segmented or just as is) to view misplacements with respect to the target regions.

7. Return to step 2 until all the seeds have been implanted.

Note that during an operation and after seed reconstruction, seed displacement, registration to ultrasound or elastography can be used independently or in any combination at the oncologists discretion. For example, an oncologist could choose to only perform an RP ultrasound sweep for registration of fluoro to ultrasound, if the average computed displacement is greater than a certain value. This could be done by relying on a good "intra-operative preplan" to assume correct placement for low displacement measurements. Figure 6.1 provides an example screen image that can be used to visualize seed displacements relative to the target regions. This would only be possible with a combination of all the methods presented in this thesis.

After an operation, data collected from all of the algorithms presented can be used to further analyze displacement trends.

6.2   Future Work

Further studies are needed to fully register seed displacements to prostate volumes. This could not be done here since two different patient studies were used for the seed displacement analysis and the absolute elastography study. For this to be possible the elastography system must be included in a study with patients undergoing brachytherapy.

The main issue with the fluoro reconstruction is the availability of real-time data to compute the seed positions from. In this work, it is assumed that the fluoro images are immediately available for real-time processing as soon as they are acquired. This is not currently the case and the images have to be imported post-operatively. This is a serious limitation but proof of the feasibility of intra-operative planning could lead to the use of machines that do allow real-time data access.

The main improvements for the target volume delineation process lie in the automation of the segmentation and in the excitation mechanism. Research is needed
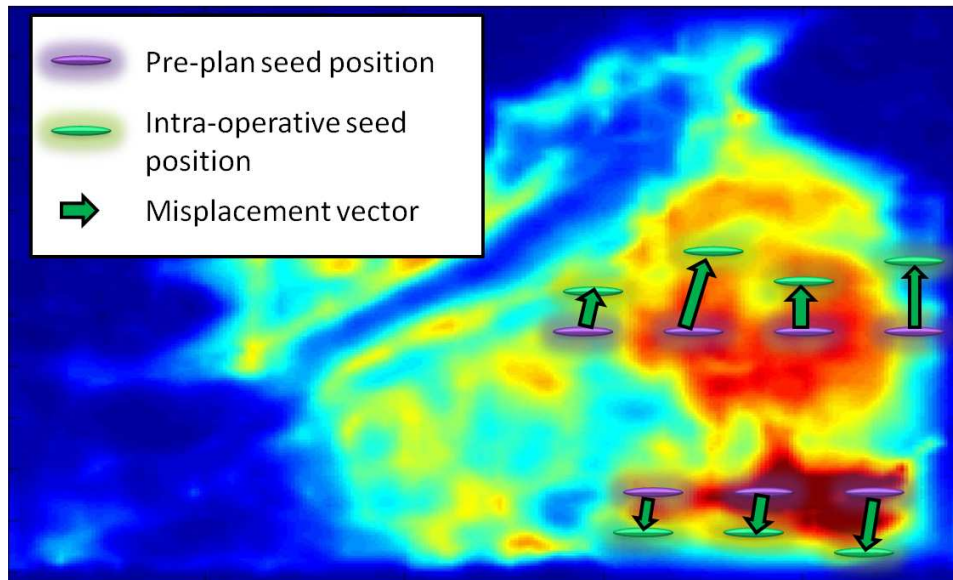
Figure 6.1: A potential intra-operative planning interface. Intra-operative seed positions and misplacement vectors are registered to and overlaid on top of an ultrasound slice. The target regions can be inferred by the oncologist due to the visual enhancement provided by the elastogram.

to develop a transperineal excitation mechanism that acts through the square-faced template guide or a transrectal excitation mechanism that is is decoupled from the TRUS probe. As for the automatic segmentation, this has been shown to work using elastography images to initialize other automatic segmentation algorithms [7, 42]. The extension of this is to then identify tumourous regions in the prostate to further aid the planning and placement process. To do this, further research is needed to determine the correlation of the stiff regions in the prostate to cancer. In addition, the effect of needle insertion on the quality of elastography results has to be investigated. Nonetheless, a intra-operative pre-plan is still possible. Even without explicit segmentation, displays such as the one in Figure 6.1 can be provided which still give an oncologist feedback on the misplacements since they can infer target regions based on expert knowledge.

Bibliography

[1] P. Abolmaesumi and M. Sirouspour. Segmentation of prostate contours from ultrasound images. In *Acoustics, Speech, and Signal Processing, 2004. Proceedings.(ICASSP'04). IEEE International Conference on*, volume 3, pages iii–517. IEEE, 2004. → pages 57, 74

[2] H. Ahmed, D. Pendse, R. Illing, C. Allen, J. van der Meulen, and M. Emberton. Will focal therapy become a standard of care for men with localized prostate cancer? *Nature Clinical Practice Oncology*, 4(11): 632–642, 2007. → pages 4, 58

[3] R. Ahuja, T. Magnanti, and J. Orlin. *Network Flows: Theory, Algorithms, and Applications*, volume 846. Prentice Hall, 2005. → pages 19

[4] M. Altschuler, P. Findlay, and R. Epperson. Rapid, accurate, three-dimensional location of multiple seeds in implant radiotherapy treatment planning. *Physics in medicine and biology*, 28(11):1305, 2000. → pages 10

[5] H. Amols and I. Rosen. A three-film technique for reconstruction of radioactive seed implants. *Medical physics*, 8:210, 1981. → pages 10

[6] L. Archambault, L. Beaulieu, and D. Tubic. Automatic post-implant needle reconstruction algorithm to characterize and improve implant robustness analyses. *Medical Physics*, 30(11):2897–2903, 2003. doi:10.1118/1.1617480. → pages 36

[7] S. Badiei, S. Salcudean, J. Varah, and W. Morris. Prostate segmentation in 2d ultrasound images using image warping and ellipse fitting. *Medical Image Computing and Computer-Assisted Intervention–MICCAI 2006*, pages 17–24, 2006. → pages 43, 54, 57, 74, 81

[8] A. Baghani, A. Brant, S. Salcudean, and R. Rohling. A high-frame-rate ultrasound system for the study of tissue motions. *Ultrasonics,*

Ferroelectrics and Frequency Control, IEEE Transactions on, 57(7): 1535–1547, 2010. → pages 59, 61, 62

[9] A. Baghani, S. Salcudean, M. Honarvar, R. Sahebjavaher, R. Rohling, and R. Sinkus. Travelling wave expansion: A model fitting approach to the inverse problem of elasticity reconstruction. *Medical Imaging, IEEE Transactions on*, 30(8):1555–65, Aug. 2011. → pages 4, 7, 58, 59, 74

[10] A. Baghani, H. Eskandari, W. Wang, D. Da Costa, M. Lathiff, R. Sahebjavaher, S. Salcudean, and R. Rohling. Real-time quantitative elasticity imaging of deep tissue using free-hand conventional ultrasound. *Medical Image Computing and Computer-Assisted Intervention–MICCAI 2012*, pages 617–624, 2012. → pages 4, 59, 60

[11] P. J. Besl and N. D. McKay. A method for registration of 3-d shapes. *IEEE Trans. Pattern Anal. Mach. Intell.*, 14:239–256, Feb. 1992. ISSN 0162-8828. doi:10.1109/34.121791. → pages 38, 43

[12] D. Beyer, R. Shapiro, and F. Puente. Real-time optimized intraoperative dosimetry for prostate brachytherapy: a pilot study. *International Journal of Radiation Oncology* Biology* Physics*, 48(5):1583–1589, 2000. → pages 4

[13] P. Biggs and D. Kelley. Geometric reconstruction of seed implants using a three-film technique. *Medical physics*, 10:701, 1983. → pages 10

[14] J. Bondy and U. Murty. *Graph theory with applications*, volume 290. Macmillan London, 1976. → pages 19

[15] N. Chng, I. Spadinger, W. Morris, N. Usmani, and S. Salcudean. Prostate brachytherapy postimplant dosimetry: Automatic plan reconstruction of stranded implants. *Brachytherapy*, 2010. → pages 19, 21, 26, 36, 40, 53

[16] E. Dehghan, A. Jain, M. Moradi, X. Wen, W. James Morris, S. Salcudean, and G. Fichtinger. Brachytherapy seed reconstruction with joint-encoded c-arm single-axis rotation and motion compensation. *Medical image analysis*, 15(5):760–771, 2011. → pages 5, 10, 16

[17] E. Dehghan, M. Moradi, X. Wen, D. French, J. Lobo, W. Morris, S. Salcudean, and G. Fichtinger. Prostate implant reconstruction from c-arm images with motion-compensated tomosynthesis. *Medical Physics*, 38:5290, 2011. → pages 17, 38, 46, 75

[18] S. Eggener, P. Scardino, P. Carroll, M. Zelefsky, O. Sartor, H. Hricak, T. Wheeler, S. Fine, J. Trachtenberg, M. Rubin, et al. Focal therapy for localized prostate cancer: a critical appraisal of rationale and modalities. *Journal of Urology*, 178(6):2260–2267, 2007. → pages 4, 58

[19] H. Eskandari, O. Goksel, S. Salcudean, and R. Rohling. Bandpass sampling of high-frequency tissue motion. *Ultrasonics, Ferroelectrics and Frequency Control, IEEE Transactions on*, 58(7):1332–1343, 2011. → pages 59, 61, 68

[20] H. M. Fagundes, R. J. Keys, M. F. Wojcik, M. A. Radden, C. G. Bertelsman, and W. A. Cavanagh. Transperineal trus-guided prostate brachytherapy using loose seeds versus rapidstrand: A dosimetric analysis. *Brachytherapy*, 3(3):136 – 140, 2004. ISSN 1538-4721. doi:10.1016/j.brachy.2004.05.006. → pages 19

[21] P. Fallavollita, Z. Aghaloo, E. Burdette, D. Song, P. Abolmaesumi, and G. Fichtinger. Registration between ultrasound and fluoroscopy or ct in prostate brachytherapy. *Medical physics*, 37:2749, 2010. → pages 5

[22] M. A. Fischler and R. C. Bolles. Random sample consensus: A paradigm for model fitting with application to image analysis and automated cartography. *Commun. ACM*, 24(6):381–395, Jun. 1981. → pages 21

[23] D. French, J. Morris, M. Keyes, and S. Salcudean. Real-time dosimetry for prostate brachytherapy using trus and fluoroscopy. *Medical Image Computing and Computer-Assisted Intervention–MICCAI 2004*, pages 983–991, 2004. → pages 5, 37

[24] M. Gao, J. Z. Wang, S. Nag, and N. Gupta. Effects of seed migration on post-implant dosimetry of prostate brachytherapy. *Medical Physics*, 34(2): 471–480, 2007. doi:10.1118/1.2409748. → pages 35

[25] R. Gewanter, C. Wuu, J. Laguna, A. Katz, and R. Ennis. Intraoperative preplanning for transperineal ultrasound-guided permanent prostate brachytherapy. *International Journal of Radiation Oncology* Biology* Physics*, 48(2):377–380, 2000. → pages 4

[26] L. Gong, S. Pathak, D. Haynor, P. Cho, and Y. Kim. Parametric shape modeling using deformable superellipses for prostate segmentation. *Medical Imaging, IEEE Transactions on*, 23(3):340–349, 2004. → pages 57

[27] B. Han, K. Wallner, G. Merrick, W. Butler, S. Sutlief, and J. Sylvester. Prostate brachytherapy seed identification on post-implant trus images. *Medical physics*, 30:898, 2003. → pages 37

[28] C. Herbert, W. J. Morris, J. Hamm, V. Lapointe, M. McKenzie, T. Pickles, I. Spadinger, and M. Keyes. The effect of loose vs. stranded seeds on biochemical no evidence of disease in patients with carcinoma of the prostate treated with iodine-125 brachytherapy. *Brachytherapy*, In Press, Corrected Proof:–, 2011. ISSN 1538-4721. doi:DOI:10.1016/j.brachy.2011.01.011. → pages 19

[29] A. Hodge, A. Fenster, D. Downey, and H. Ladak. Prostate boundary segmentation from ultrasound images using 2d active shape models: Optimisation and extension to 3d. *Computer methods and programs in biomedicine*, 84(2-3):99–113, 2006. → pages 57, 74

[30] D. Jaffray, J. Siewerdsen, G. Edmundson, J. Wong, and A. Martinez. Flat-panel cone-beam ct on a mobile isocentric c-arm for image-guided brachytherapy. *Flat-panel cone-beam CT on a mobile isocentric C-arm for image-guided brachytherapy, Proc. SPIE*, 4682:209–217, 2002. → pages 3

[31] A. Jain, Y. Zhou, T. Mustufa, E. Burdette, G. Chirikjian, and G. Fichtinger. Matching and reconstruction of brachytherapy seeds using the hungarian algorithm (marshal). *Medical physics*, 32:3475, 2005. → pages 5, 9

[32] B. Jian and B. Vemuri. A robust algorithm for point set registration using mixture of gaussians. In *Computer Vision, 2005. ICCV 2005. Tenth IEEE International Conference on*, volume 2, pages 1246–1251. IEEE, 2005. → pages 43

[33] I. D. Kaplan, P. M. Meskell, M. Lieberfarb, B. Saltzman, S. Berg, and E. J. Holupka. A comparison of the precision of seeds deposited as loose seeds versus suture embedded seeds: A randomized trial. *Brachytherapy*, 3(1): 7–9, 2004. doi:10.1016/j.brachy.2003.12.003. → pages 35

[34] M. G. Kay and A. N. Parlikad. Material flow analysis of public logistics networks. *Progress in Material Handling Research*, pages 205–218, 2002. → pages 27

[35] H. Knutsson, C. Westin, and G. Granlund. Local multiscale frequency and bandwidth estimation. In *Image Processing, 1994. Proceedings. ICIP-94., IEEE International Conference*, volume 1, pages 36–40. IEEE, 1994. → pages 59

[36] H. Kolsky. Stress waves in solids. *Journal of sound and Vibration*, 1(1): 88–110, 1964. → pages 58

[37] R. Kon, A. Kumar Jain, and G. Fichtinger. Hidden seed reconstruction from c-arm images in brachytherapy. In *Biomedical Imaging: Nano to Macro, 2006. 3rd IEEE International Symposium on*, pages 526–529. IEEE, 2006. → pages 17

[38] K. KÖNIG, U. Scheipers, A. Pesavento, A. Lorenz, H. Ermert, and T. Senge. Initial experiences with real-time elastography guided biopsies of the prostate. *The Journal of urology*, 174(1):115–117, 2005. → pages 4, 58

[39] T. Krouskop, T. Wheeler, F. Kallel, B. Garra, T. Hall, et al. Elastic moduli of breast and prostate tissues under compression. *Ultrasonic imaging*, 20(4): 260, 1998. → pages 4, 58

[40] V. Lagerburg, M. Moerland, J. Lagendijk, and J. Battermann. Measurement of prostate rotation during insertion of needles for brachytherapy. *Radiotherapy and Oncology*, 77(3):318–323, 2005. → pages 2, 53

[41] J. Lee, C. Labat, A. Jain, D. Song, E. Burdette, G. Fichtinger, and J. Prince. Redmaps: Reduced-dimensionality matching for prostate brachytherapy seed reconstruction. *Medical Imaging, IEEE Transactions on*, 30(1):38–51, 2011. → pages 5

[42] S. Mahdavi and S. Salcudean. 3d prostate segmentation based on ellipsoid fitting, image tapering and warping. In *Engineering in Medicine and Biology Society, 2008. EMBS 2008. 30th Annual International Conference of the IEEE*, pages 2988–2991. IEEE, 2008. → pages 57, 74, 81

[43] S. Mahdavi, M. Moradi, W. Morris, S. Goldenberg, and S. Salcudean. Fusion of ultrasound b-mode and vibro-elastography images for automatic 3d segmentation of the prostate. *Medical Imaging, IEEE Transactions on*, 2012. → pages 58

[44] C. Mathers, D. Fat, and J. Boerma. *The global burden of disease: 2004 update*. World Health Organization, 2008. → pages 1

[45] M. Mazonakis, J. Damilakis, H. Varveris, P. Prassopoulos, and N. Gourtsoyiannis. Image segmentation in treatment planning for prostate cancer using the region growing technique. *British journal of radiology*, 74 (879):243–249, 2001. → pages 57, 74

[46] G. S. Merrick, W. M. Butler, A. T. Dorsey, J. H. Lief, and M. L. Benson. Seed fixity in the prostate/periprostatic region following brachytherapy. *International Journal of Radiation Oncology Biology Physics*, 46(1): 215–220, Jan. 2000. doi:10.1016/S0360-3016(99)00405-8. → pages 35

[47] E. Messing, J. Zhang, D. Rubens, R. Brasacchio, J. Strang, A. Soni, M. Schell, P. Okunieff, and Y. Yu. Intraoperative optimized inverse planning for prostate brachytherapy: Early experience. *International Journal of Radiation Oncology* Biology* Physics*, 44(4):801–808, 1999. → pages 4, 57

[48] M. Moradi, S. Mahdavi, E. Dehghan, J. Lobo, S. Deshmukh, W. Morris, G. Fichtinger, and S. Salcudean. Seed localization in ultrasound and registration to c-arm fluoroscopy using matched needle tracks for prostate brachytherapy. *Biomedical Engineering, IEEE Transactions on*, 59(9): 2558–2567, 2012. → pages xi, 5, 7, 9, 10, 12, 37, 38, 43, 50, 54

[49] W. Morris, M. Keyes, D. Palma, I. Spadinger, M. McKenzie, A. Agranovich, T. Pickles, M. Liu, W. Kwan, and J. Wu. Population-based study of biochemical and survival outcomes after permanent 125I brachytherapy for low- and intermediate-risk prostate cancer. *Urology*, 73(4):860–865, Apr. 2009. doi:10.1016/j.urology.2008.07.064. → pages 1

[50] S. Muto, T. Yoshii, K. Saito, Y. Kamiyama, H. Ide, and S. Horie. Focal therapy with high-intensity-focused ultrasound in the treatment of localized prostate cancer. *Japanese journal of clinical oncology*, 38(3):192–199, 2008. → pages 4, 58

[51] S. Nag, W. Bice, K. DeWyngaert, B. Prestidge, R. Stock, and Y. Yu. The american brachytherapy society recommendations for permanent prostate brachytherapy postimplant dosimetric analysis. *Int J Radiat Oncol Biol Phys*, 46(1):221–30, Jan. 2000. ISSN 0360-3016. doi:10.1016/S0360-3016(99)00351-X. → pages 4

[52] S. Nag, J. Ciezki, R. Cormack, S. Doggett, K. DeWyngaert, G. Edmundson, R. Stock, N. Stone, Y. Yu, M. Zelefsky, et al. Intraoperative planning and evaluation of permanent prostate brachytherapy: report of the american brachytherapy society. *International journal of radiation oncology, biology, physics*, 51(5):1422–1430, 2001. → pages 2, 4, 56, 78, 79

[53] E. Nelson, C. Slotoroff, L. Gomella, and E. Halpern. Targeted biopsy of the prostate: the impact of color doppler imaging and elastography on prostate cancer detection and gleason score. *Urology*, 70(6):1136–1140, 2007. → pages 58

[54] J. Ophir, I. Cespedes, H. Ponnekanti, Y. Yazdi, and X. Li. Elastography: a quantitative method for imaging the elasticity of biological tissues. *Ultrasonic imaging*, 13(2):111–134, 1991. → pages 4, 58

[55] P. Orio, I. Tutar, S. Narayanan, S. Arthurs, P. Cho, Y. Kim, G. Merrick, and K. Wallner. Intraoperative ultrasound-fluoroscopy fusion can enhance prostate brachytherapy quality. *International Journal of Radiation Oncology* Biology* Physics*, 69(1):302–307, 2007. → pages 4

[56] L. Pallwein, M. Mitterberger, P. Struve, G. Pinggera, W. Horninger, G. Bartsch, F. Aigner, A. Lorenz, F. Pedross, and F. Frauscher. Real-time elastography for detecting prostate cancer: preliminary experience. *BJU international*, 100(1):42–46, 2007. → pages 4, 58

[57] M. Pinkawa, B. Gagel, B. Asadpour, M. Piroth, J. Klotz, H. Borchers, G. Jakse, and M. Eble. Seed displacements after permanent brachytherapy for prostate cancer in dependence on the prostate level. *Strahlentherapie und Onkologie*, 184(10):520–525, Oct. 2008. ISSN 0179-7158. doi:10.1007/s00066-008-1886-3. → pages 36

[58] M. Pinkawa, B. Asadpour, M. D. Piroth, B. Gagel, J. Klotz, K. Fischedick, H. Borchers, G. Jakse, and M. J. Eble. Rectal dosimetry following prostate brachytherapy with stranded seeds - comparison of transrectal ultrasound intra-operative planning (day 0) and computed tomography-postplanning (day 1 vs. day 30) with special focus on sources placed close to the rectal wall. *Radiotherapy and Oncology*, 91(2):207–212, May. 2009. ISSN 0167-8140. doi:10.1016/j.radonc.2008.11.012. → pages 36

[59] A. Polo, C. Salembier, J. Venselaar, and P. Hoskin. Review of intraoperative imaging and planning techniques in permanent seed prostate brachytherapy. *Radiotherapy and Oncology*, 94(1):12 – 23, 2010. ISSN 0167-8140. doi:10.1016/j.radonc.2009.12.012. → pages 2, 4

[60] D. R. Reed, K. E. Wallner, G. S. Merrick, S. Arthurs, A. Mueller, W. Cavanagh, W. B. Butler, E. Ford, and S. G. Sutlief. A prospective randomized comparison of stranded vs. loose 125I seeds for prostate brachytherapy. *Brachytherapy*, 6(2):129 – 134, Apr. 2007. ISSN 1538-4721. doi:10.1016/j.brachy.2007.01.003. → pages 19

[61] P. L. Roberson, N. Vrinda, L. M. Daniel, J. W. Raymond, and P. W. McLaughlin. Source placement error for permanent implant of the prostate. *Med. Phys.*, 24b(2):251–257, Feb. 1997. doi:10.1118/1.598058. → pages 35

[62] M. Rosenthal and R. Nath. Automatic seed identification technique for interstitial implants using three isocentric radiographs. *Med. Phys.;(United States)*, 10(4), 1983. → pages 10

[63] G. Salomon, J. Köllerman, I. Thederan, F. Chun, L. Budäus, T. Schlomm, H. Isbarn, H. Heinzer, H. Huland, and M. Graefen. Evaluation of prostate cancer detection with ultrasound real-time elastography: a comparison with step section pathological analysis after radical prostatectomy. *European urology*, 54(6):1354–1362, 2008. → pages 4, 58

[64] J. Shah, C. Wuu, A. Katz, J. Laguna, M. Benson, and R. Ennis. Improved biochemical control and clinical disease-free survival with intraoperative versus preoperative preplanning for transperineal interstitial permanent prostate brachytherapy. *The Cancer Journal*, 12(4):289–297, 2006. → pages 4

[65] G. Sherouse, K. Novins, and E. Chaney. Computation of digitally reconstructed radiographs for use in radiotherapy treatment design. *International Journal of Radiation Oncology* Biology* Physics*, 18(3): 651–658, 1990. → pages 37

[66] J. Siewerdsen, D. Moseley, S. Burch, S. Bisland, A. Bogaards, B. Wilson, and D. Jaffray. Volume ct with a flat-panel detector on a mobile, isocentric c-arm: pre-clinical investigation in guidance of minimally invasive surgery. *Medical physics*, 32:241, 2005. → pages 3

[67] Y. Su, B. Davis, M. Herman, and R. Robb. Prostate brachytherapy seed localization by analysis of multiple projections: Identifying and addressing the seed overlap problem. *Medical physics*, 31:1277, 2004. → pages 5

[68] Y. Su, B. Davis, K. Furutani, M. Herman, and R. Robb. Seed localization and trus-fluoroscopy fusion for intraoperative prostate brachytherapy dosimetry. *Computer Aided Surgery*, 12(1):25–34, 2007. → pages 5, 37

[69] Y. Su, B. J. Davis, K. M. Furutani, M. G. Herman, and R. A. Robb. Dosimetry accuracy as a function of seed localization uncertainty in permanent prostate brachytherapy: increased seed number correlates with less variability in prostate dosimetry. *Physics in Medicine and Biology*, 52 (11):3105, Jun. 2007. doi:10.1088/0031-9155/52/11/012. → pages 53

[70] O. Tanaka, S. Hayashi, M. Matsuo, M. Nakano, Y. Kubota, S. Maeda, K. Ohtakara, T. Deguchi, and H. Hoshi. Mri-based preplanning in low-dose-rate prostate brachytherapy. *Radiotherapy and Oncology*, 88(1): 115–120, 2008. → pages 3

[71] R. Taschereau, J. Roy, and J. Pouliot. Monte carlo simulations of prostate implants to improve dosimetry and compare planning methods. *Med. Phys.*, 26(9):1952–1959, 1999. → pages 35

[72] C. Tempany, S. Straus, N. Hata, and S. Haker. Mr-guided prostate interventions. *Journal of Magnetic Resonance Imaging*, 27(2):356–367, 2008. → pages 3

[73] D. Tubic, A. Zaccarin, L. Beaulieu, and J. Pouliot. Automated seed detection and three-dimensional reconstruction. ii. reconstruction of permanent prostate implants using simulated annealing. *Medical physics*, 28:2272, 2001. → pages 5

[74] D. Tubic, A. Zaccarin, J. Pouliot, and L. Beaulieu. Automated seed detection and three-dimensional reconstruction. i. seed localization from fluoroscopic images or radiographs. *Medical physics*, 28:2265, 2001. → pages

[75] I. Tutar, R. Managuli, V. Shamdasani, P. Cho, S. Pathak, and Y. Kim. Tomosynthesis-based localization of radioactive seeds in prostate brachytherapy. *Medical physics*, 30:3135, 2003. → pages 5, 37

[76] I. Tutar, S. Narayanan, H. Lenz, R. Nurani, P. Orio, P. Cho, K. Wallner, and Y. Kim. Seed-based ultrasound and fluoroscopy registartion using iterative optimal assignment for intraoperative prostate brachytherapy dosimetry. In *Proceedings of SPIE Medical Imaging*, volume 6509, page 650914, 2007. → pages 37

[77] N. Usmani, N. Chng, I. Spadinger, and W. J. Morris. Lack of significant intraprostatic migration of stranded iodine-125 sources in prostate brachytherapy implants. *Brachytherapy*, In Press, Corrected Proof:–, 2010. ISSN 1538-4721. doi:DOI:10.1016/j.brachy.2010.10.001. → pages 36, 38

[78] S. Vesely, T. Knutson, J. Damber, M. Dicuio, and C. Dahlstrand. Relationship between age, prostate volume, prostate-specific antigen, symptom score and uroflowmetry in men with lower urinary tract symptoms. *Scandinavian journal of urology and nephrology*, 37(4):322–328, 2003. → pages 73

[79] G. Wan, Z. Wei, L. Gardi, D. B. Downey, and A. Fenster. Brachytherapy needle deflection evaluation and correction. *Medical Physics*, 32(4): 902–909, 2005. → pages 53

[80] X. Wen and S. Salcudean. Detection of brachytherapy seeds using 3d ultrasound. In *Engineering in Medicine and Biology Society, 2008. EMBS 2008. 30th Annual International Conference of the IEEE*, pages 855–858. IEEE, 2008. → pages 10, 43

[81] D. Wilkinson, E. Lee, J. Ciezki, D. Mohan, C. Zippe, K. Angermeier, J. Ulchaker, and E. Klein. Dosimetric comparison of pre-planned and or-planned prostate seed brachytherapy. *International Journal of Radiation Oncology* Biology* Physics*, 48(4):1241–1244, 2000. → pages 4

[82] J. Xue, F. Waterman, J. Handler, and E. Gressen. Localization of linked¡ sup¿ 125¡/sup¿ i seeds in postimplant trus images for prostate brachytherapy dosimetry. *International Journal of Radiation Oncology* Biology* Physics*, 62(3):912–919, 2005. → pages 37

[83] Y. Yamada, L. Potters, M. Zaider, G. Cohen, E. Venkatraman, and M. Zelefsky. Impact of intraoperative edema during transperineal permanent prostate brachytherapy on computer-optimized and preimplant planning techniques. *American journal of clinical oncology*, 26(5):e130, 2003. → pages 2

[84] L. Zollei, E. Grimson, A. Norbash, and W. Wells. 2d-3d rigid registration of x-ray fluoroscopy and ct images using mutual information and sparsely sampled histogram estimators. In *Computer Vision and Pattern Recognition, 2001. CVPR 2001. Proceedings of the 2001 IEEE Computer Society Conference on*, volume 2, pages II–696. IEEE, 2001. → pages 37